

Supplementary Information for

Engineering Molecular Ruthenium Catalyst into Three-Dimensional Metal Covalent Organic Frameworks for Efficient Water Oxidation

Wang-Kang Han,^a Yong Liu,^a Jing-Dong Feng,^a Xiaodong Yan,^a Huan Pang^b and Zhi-Guo Gu^{*a}

[a] W.-K Han, Y. Liu, J.-D Feng, Prof. Dr. X. Yan, Prof. Dr. Z.-G Gu

Key Laboratory of Synthetic and Biological Colloids, Ministry of Education, School of
Chemical and Material Engineering

Jiangnan University

Wuxi 214122, China

[b] Prof. Dr. H. Pang

School of Chemistry and Chemical Engineering,

Yangzhou University

Yangzhou 225002, China

**E-mail: zhiguogu@jiangnan.edu.cn*

Table of Contents

Section 1. Materials and methods	3
1.1 Materials	3
1.2 General methods	3
Section 2. General synthetic procedures and characterizations.....	5
2.1 Synthesis and characterizations of Ru(bpy-CHO) ₂ Cl ₂	5
2.2 X-ray single crystal structure of Ru(bpy-CHO) ₂ Cl ₂	8
2.3 The model reaction	10
2.4 X-ray single crystal structure of model compound Ru(bpy-Ph) ₂ Cl ₂	12
2.5 Synthesis of RuCOFs	14
2.6 FT-IR analysis	15
2.7 Solid-state ¹³ C NMR spectra	16
2.8 Chemical stability	17
2.9 Thermogravimetric analysis	18
2.10 High resolution transmission electron microscopy (HRTEM).....	18
2.11 XPS analysis.....	20
Section 3. PXRD analysis and structural modeling of the RuCOFs	21
3.1 Comparison of PXRD patterns for RuCOFs and their related monomers	21
3.2 Structural modeling of the RuCOFs	21
3.3 PXRD analysis of the RuCOFs with substituting the Cl ligands	29
Section 4. Water oxidation experiments	30
4.1 Oxygen evolution measurements	30
4.2 Water contact angle tests	31
4.3 Water oxidation performance	32
4.4 Computational models and methods	37
4.5 Comparison of photocatalytic O ₂ evolution activity	41
4.6 Electrochemical O ₂ evolution activity.....	42
Section 5. Oxidation of organic substrates	43
5.1 Typical procedure for selective oxidation of sp ³ C-H bonds	43
5.2 Catalytic performance for selective oxidation of sp ³ C-H bonds	44
Section 6. Unit cell parameters and fractional atomic coordinates	54
Section 7. References	59

Section 1. Materials and methods

1.1 Materials

All commercially available starting compounds and solvents were purchased from commercial sources and used without further purification. The organic building units 4,4',4'',4'''-(ethene-1,1,2,2-tetrayl)tetraaniline (ETTA) and 4',4''',4''''',4''''''-(ethene-1,1,2,2-tetrayl)tetrakis((1,1'-biphenyl)-4-amine) (ETTBA) were synthesized according to the reported procedures.^[1,2]

1.2 General methods

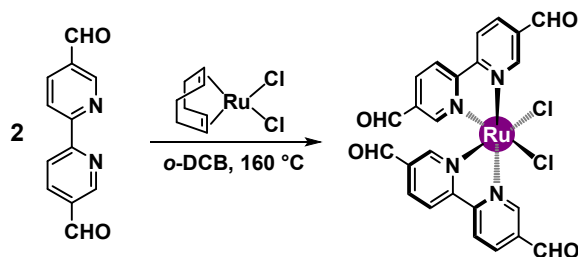
Fourier transform infrared (FT-IR) spectra were collected on a Nicolet 6700 FT-IR spectrophotometer with ATR attachment. Solution ¹H and ¹³C nuclear magnetic resonance (NMR) spectra were recorded on AVANCE III NMR instrument at 298 K using standard Bruker software, and chemical shifts were reported in parts per milion (ppm) downfield from tetramethylsilane. Solid-state ¹³C cross-polarization magic-angle spinning (CP-MAS) NMR experiments were performed on a Bruker Avance III HD spectrometer. Electrospray ionization mass spectrometry (ESI-MS) spectra were recorded using a Waters Quattro Premier XE. Elemental analysis was collected using an Elementar Vario EL cube under CHN model. X-ray photoelectron spectroscopy (XPS) measurements were carried out on an AXIS Supra by Kratos Analytical Inc. using monochromatized Al K α radiation ($h\nu = 1486.6$ eV) as X-ray source. All XPS spectra were calibrated by C1s signal at 284.8 eV. Thermogravimetric analyses (TGA) were carried out using TGA/1100SF thermo gravimetric analyzer. The nitrogen sorption isotherms and pore-size distribution curves were measured at 77 K using Micromeritics ASAP 2010 equipment. The morphology and microstructure of the products were characterized by using scanning electron microscopy (SEM, HitachiS-4800) and transmission electron microscope (TEM, FEI Tecnai G2 F20). Inductively coupled plasma optical emission spectrometry (ICP-OES) measurements were carried out by using Agilent 5110. The samples were prepared via digestion by nitrohydrochloric acid, and then diluted using distilled water. Powder X-ray diffraction (PXRD) patterns were collected on a D8 Advance X-ray diffractometer (Bruker AXS Germany) with Cu K α radiation at room temperature. The small angle X-ray scattering (SAXS) measurements were performed using two-dimensional multifunctional small Angle X-ray scatterer (Xeuss 3.0) equipped with a Cu microfocus sealed tube (30 W/30 μ m). Foxtrot software was used for the data reduction with normalized circle gathering. Water contact angle measurements were performed by using a drop shape analysis apparatus (OCA15EC). The powder samples were tested by pressed into thin discs in a stainless-steel spacer with controlled mass amounts (30 mg) at 15 MPa for 2 min. The water contact angles were analyzed by using the LBADSA method with the ImageJ software. The electrochemical measurements were recorded on the CHI660E electrochemical workstation with a standard three-electrode system with the catalyst-coated ITO as the

working electrode, Pt plate as the counter electrode and the Ag/AgCl electrode (saturated KCl) as the reference electrode. A phosphate buffer solution (pH = 7) was used as the electrolyte.

The single-crystal X-ray data of Ru(bpy-CHO)₂Cl₂ was collected on a Bruker APEX-II CCD diffractometer with graphite monochromatic Mo *K*α radiation ($\lambda = 0.71073 \text{ \AA}$). The data was collected at 150 K. The single-crystal X-ray data of the model compound Ru(bpy-Ph)₂Cl₂ was collected on a Bruker D8 VENTURE Metaljet PHOTON II diffractometer with Helios Multi-layer Optic monochromatic Ga *K*α radiation ($\lambda = 1.34139 \text{ \AA}$). The data was collected at 193 K. Using *Olex2*,^[3] the crystal structures were solved with the *ShelXT*^[4] structure solution program using Intrinsic Phasing and refined with the *ShelXL*^[5] refinement package using Least Squares minimization. All of the non-hydrogen atoms except the anions were refined with anisotropic thermal displacement coefficients. Hydrogen atoms of organic ligands were located geometrically and refined in a riding model.

Section 2. General synthetic procedures and characterizations

2.1 Synthesis and characterizations of Ru(bpy-CHO)₂Cl₂



The synthesis of metal complex Ru(bpy-CHO)₂Cl₂ (bpy-CHO = 2,2'-bipyridine-5,5'-dicarbaldehyde) was as follow:

Typically, in a 100 mL round bottom flask, 2,2'-bipyridine-5,5'-dicarbaldehyde (509 mg, 2.4 mmol) and Ru(cyclo-octadiene)Cl₂ polymer (336.18 mg, 1.2 mmol) were suspended in 50 mL *o*-dichlorobenzene. The resulting mixture was argon degassed for three times and stirred under argon atmosphere at 160 °C for 3 h. After cooling to room temperature, the solution was precipitated by the addition of diethyl ether. Then, the resulting solid was filtered and further stirred in H₂O for 6 hours to remove any charged impurities. The dark green solid was filtered, washed with diethyl ether, and was recrystallized from CH₃CN/diethyl ether to give the pure product. The dark green crystal was obtained by slow diffusion of diethyl ether into the CH₃CN solution of Ru(bpy-CHO)₂Cl₂ at room temperature. Yield: 87%. ¹H NMR (400 MHz, DMSO-d₆, δ: ppm) 10.46 (d, 2H), 10.33 (s, 2H), 9.77 (s, 6H), 9.04 (d, 2H), 8.86 (d, 2H), 8.59 (dd, 2H), 8.13 (d, 2H), 8.11 (s, 2H). ¹³C NMR (101 MHz, DMSO-d₆, δ: ppm) 191.78, 191.34, 164.04, 162.16, 155.57, 135.51, 132.90, 132.65, 131.19, 129.33, 125.56, 125.06. ESI-MS, m/z Calcd. for C₂₄H₁₆N₄O₄RuCl₂ [M-Cl]⁺ 560.99, found: 560.98.

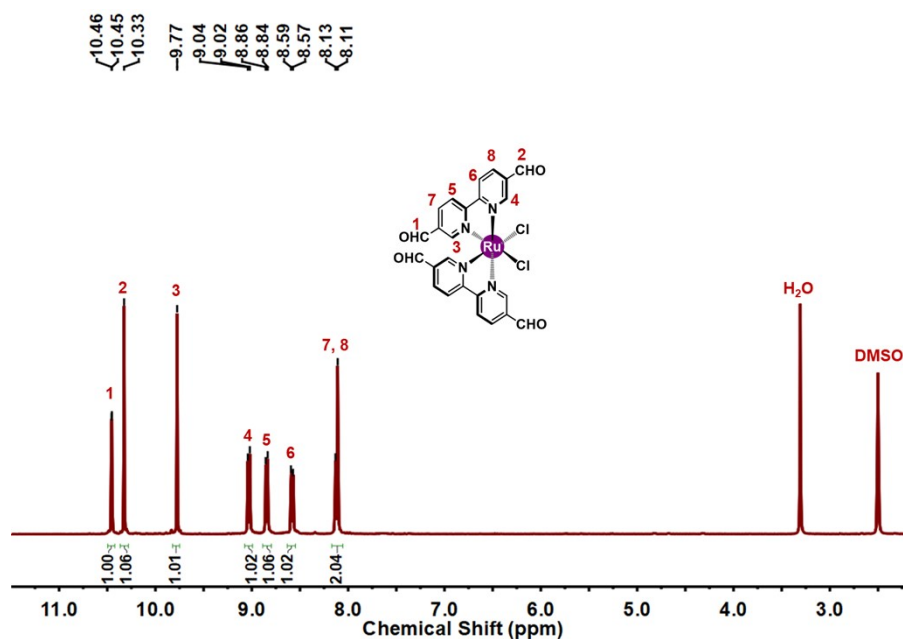


Fig. S1 ¹H NMR spectrum of Ru(bpy-CHO)₂Cl₂.

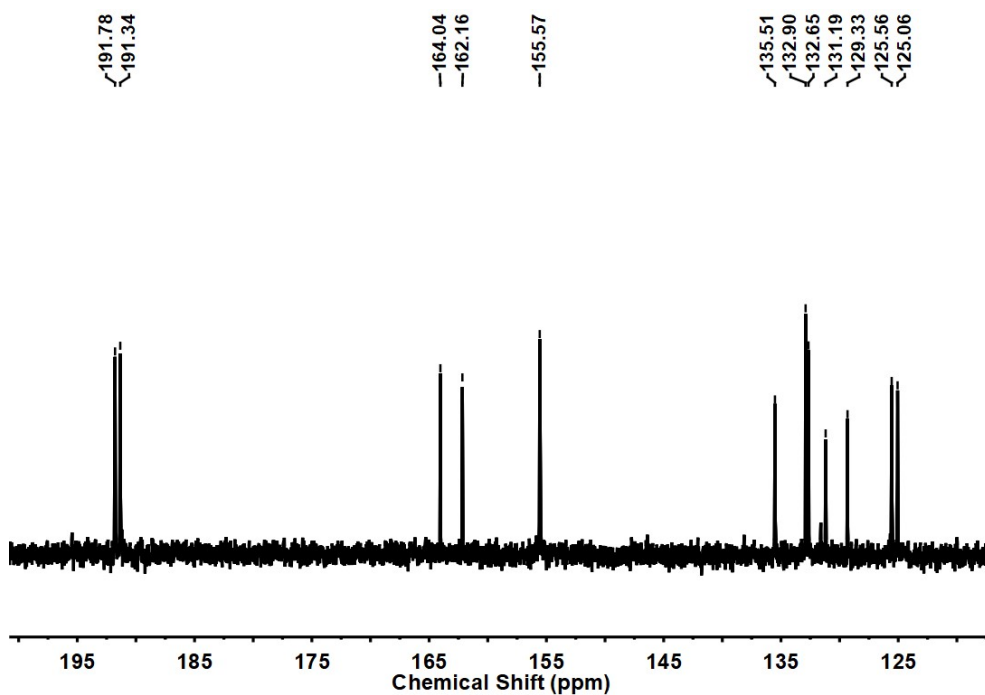


Fig. S2 ^{13}C NMR spectrum of $\text{Ru}(\text{bpy-CHO})_2\text{Cl}_2$.

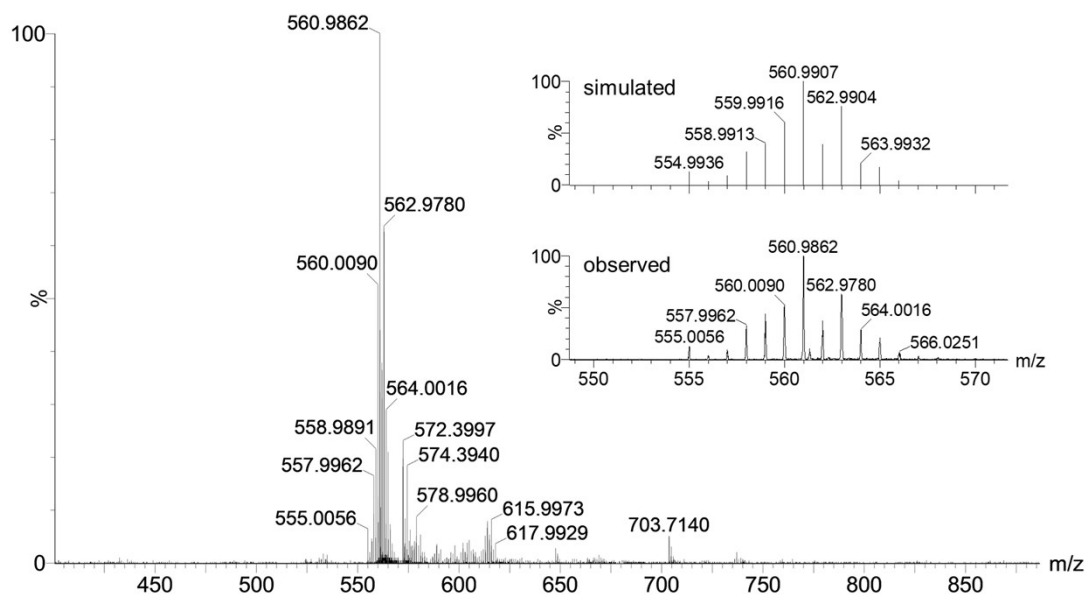


Fig. S3 ESI-MS spectrum of $\text{Ru}(\text{bpy-CHO})_2\text{Cl}_2$ with observed and simulated +1 isotopic peak distributions $[\text{M-Cl}]^+$.

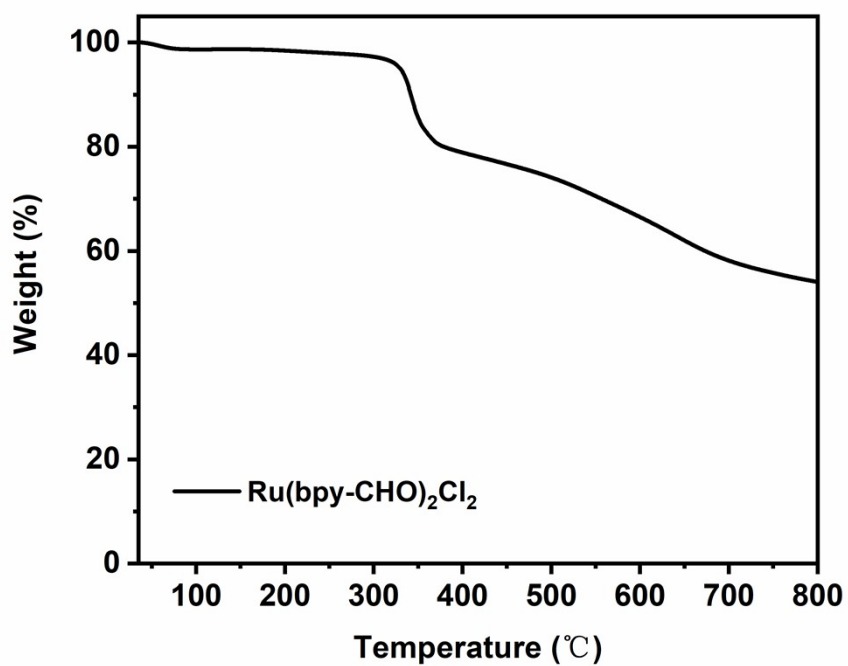


Fig. S4 Thermogravimetric analysis of Ru(bpy-CHO)₂Cl₂.

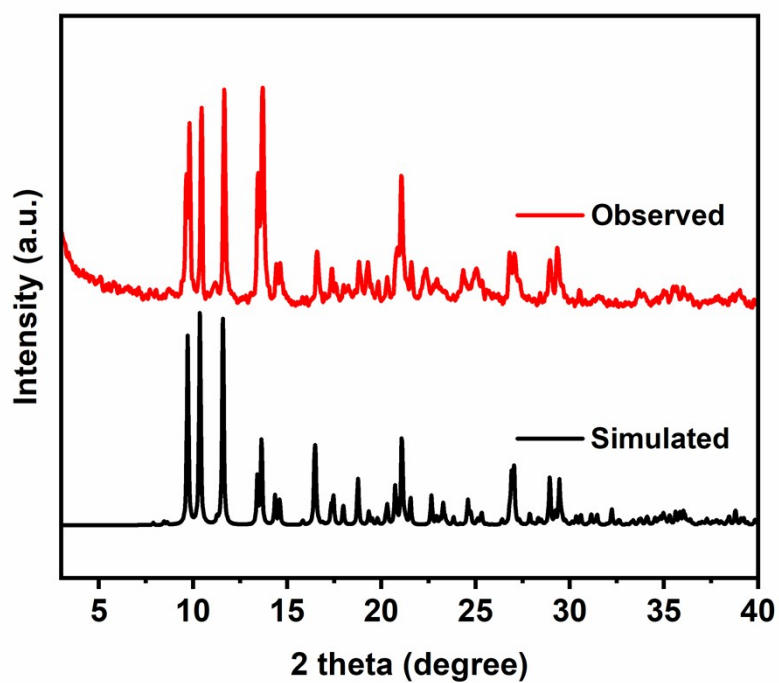


Fig. S5 Powder X-ray diffraction of the as-synthesized sample and single-crystal simulation of Ru(bpy-CHO)₂Cl₂, confirming the phase purity of our sample.

2.2 X-ray single crystal structure of Ru(bpy-CHO)₂Cl₂

Single-crystal X-ray diffraction data reveals that Ru(bpy-CHO)₂Cl₂ crystallizes in the triclinic *P*-1 space group. The Ru(II) centre is in a typical distorted octahedral geometry. Each Ru(II) coordinate with four nitrogen atoms from two bipyridine derived ligands, another two chloride anions also coordinate with the Ru(II) centre for charge balance. The average Ru-N bond length is 2.041 Å, and the average Ru-Cl bond length is 2.291 Å. The crystal structure proved that Ru(bpy-CHO)₂Cl₂ can be used as a 4-connected building unit for constructing MCOFs. The single crystal X-ray structure of Ru(bpy-CHO)₂Cl₂ also showed that the two linear bipyridine derived ligands were posited in two approximately parallel geometrical planes. In a top view, the intersection angle between the two linear bipyridine derived units is 60.3° with distorted rectangular shape. Final crystallographic data for Ru(bpy-CHO)₂Cl₂ is listed in Table S1. CCDC: 2270378.

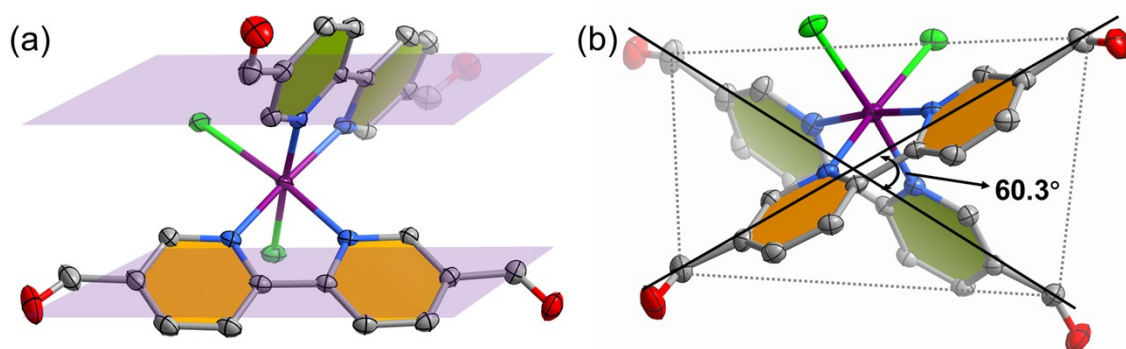
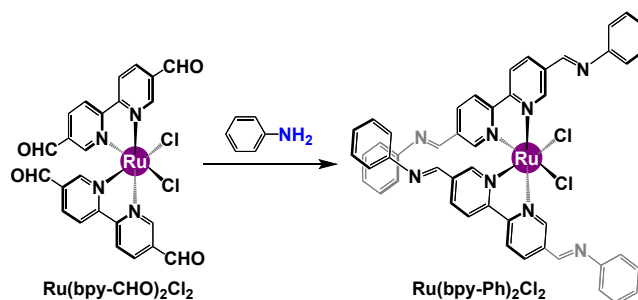


Fig. S6 The single crystal X-ray structure for Ru(bpy-CHO)₂Cl₂ (ORTEP, 30% ellipsoids): (a) Two linear bipyridine derived ligands were posited in two approximately parallel geometrical planes. (b) The intersection angle between the two linear bipyridine derived units is 60.3° with distorted rectangular shape. All H atoms and solvent molecules have been removed for clarity (C: Grey; N: blue; Ru: purple; O: red).

Table S1 Summary of crystallographic data for Ru(bpy-CHO)₂Cl₂

Ru(bpy-CHO) ₂ Cl ₂	
Formula	C ₂₄ H ₁₆ Cl ₂ N ₄ O ₄ Ru, C ₂ H ₃ N
Formula Weight	637.43
<i>T</i> (K)	150
λ (Å)	0.71073
Crystal system	triclinic
Space group	<i>P</i> -1
<i>a</i> (Å)	10.8691(3)
<i>b</i> (Å)	11.2102(3)
<i>c</i> (Å)	11.8287(3)
α (°)	71.074
β (°)	84.694
γ (°)	73.669
<i>V</i> (Å ³)	1308.34
<i>Z</i>	2
<i>D</i> _{calc} (Mg/m ³)	1.618
μ (mm ⁻¹)	0.846
<i>F</i> (000)	640
θ (°)	1.8 - 26.4
	-13 ≤ <i>h</i> ≤ 13
Index ranges	-13 ≤ <i>k</i> ≤ 14
	-14 ≤ <i>l</i> ≤ 13
Reflections collected	4845
GOF (<i>F</i> ²)	1.045
<i>R</i> ₁ ^a , <i>wR</i> ₂ ^b (<i>I</i> >2σ(<i>I</i>))	0.0302, 0.0780
<i>R</i> ₁ ^a , <i>wR</i> ₂ ^b (all data)	0.0343, 0.0747
$R_1^a = \frac{\sum F_o }{\sum F_c } - \frac{ F_c }{\sum F_o } \quad wR_2^b = \left[\frac{\sum w(F_o^2 - F_c^2)^2}{\sum w(F_o^2)} \right]^{1/2}$	

2.3 The model reaction



The metal complex building unit $\text{Ru}(\text{bpy-CHO})_2\text{Cl}_2$ (23.86 mg, 0.04 mmol) and 4.0 eq aniline (14.9 mg, 0.16 mmol) were dissolved in a mixed solvent of 0.5 mL 1,4-dioxane, 0.5 mL mesitylene, 0.2 mL acetonitrile and 0.4 mL 6M aqueous acetic acid in a pyrex tube. Then, the pyrex tube was flash frozen in a liquid N_2 bath and degassed by freeze-pump-thaw technique for three times and sealed under vacuum. Upon warming to room temperature, the tube was placed in an oven and heated at 120 °C for 24 hours. After cooling to room temperature, dark green solid was formed on the bottom of the pyrex tube, which was filtered and analyzed via ESI-MS. Meanwhile, the resulting solid was dissolved in a $\text{CH}_3\text{CN}/\text{DMF}$ solution, and dark green crystals were obtained by slow diffusion of diethyl ether into the solution. The dark green crystals were further analyzed by single-crystal X-ray diffraction.

The ESI-MS spectra showed ion peaks of the corresponding intermediate and final products, which were agreed very well with the simulated isotopic patterns (Figs. S7 and S8). These results clearly indicated the $\text{Ru}(\text{bpy-CHO})_2\text{Cl}_2$ building unit is stable in the above solvothermal condition.

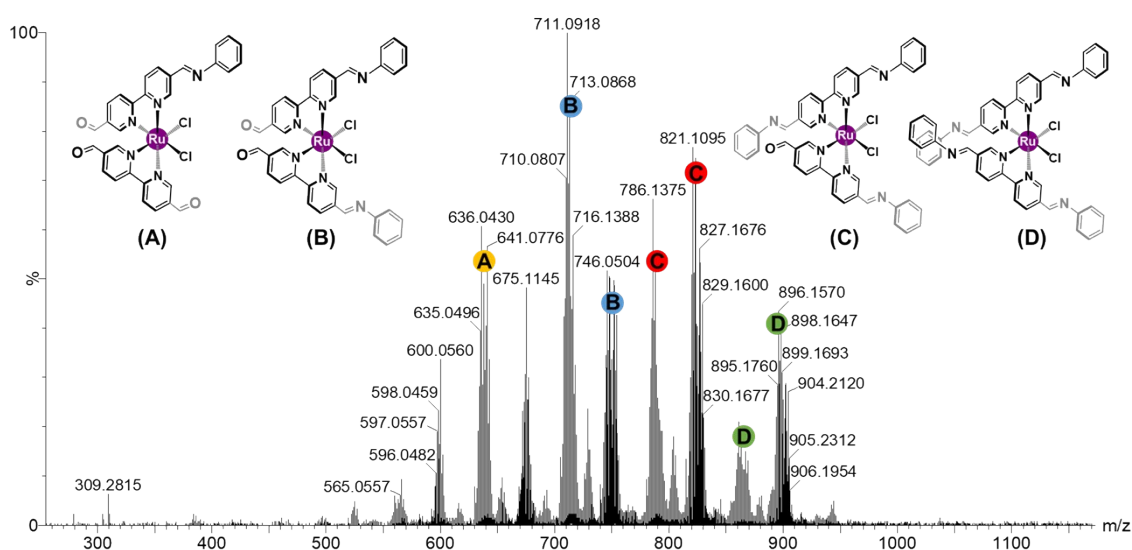


Fig. S7 The ESI-MS spectra for the isolated product of the model reaction.

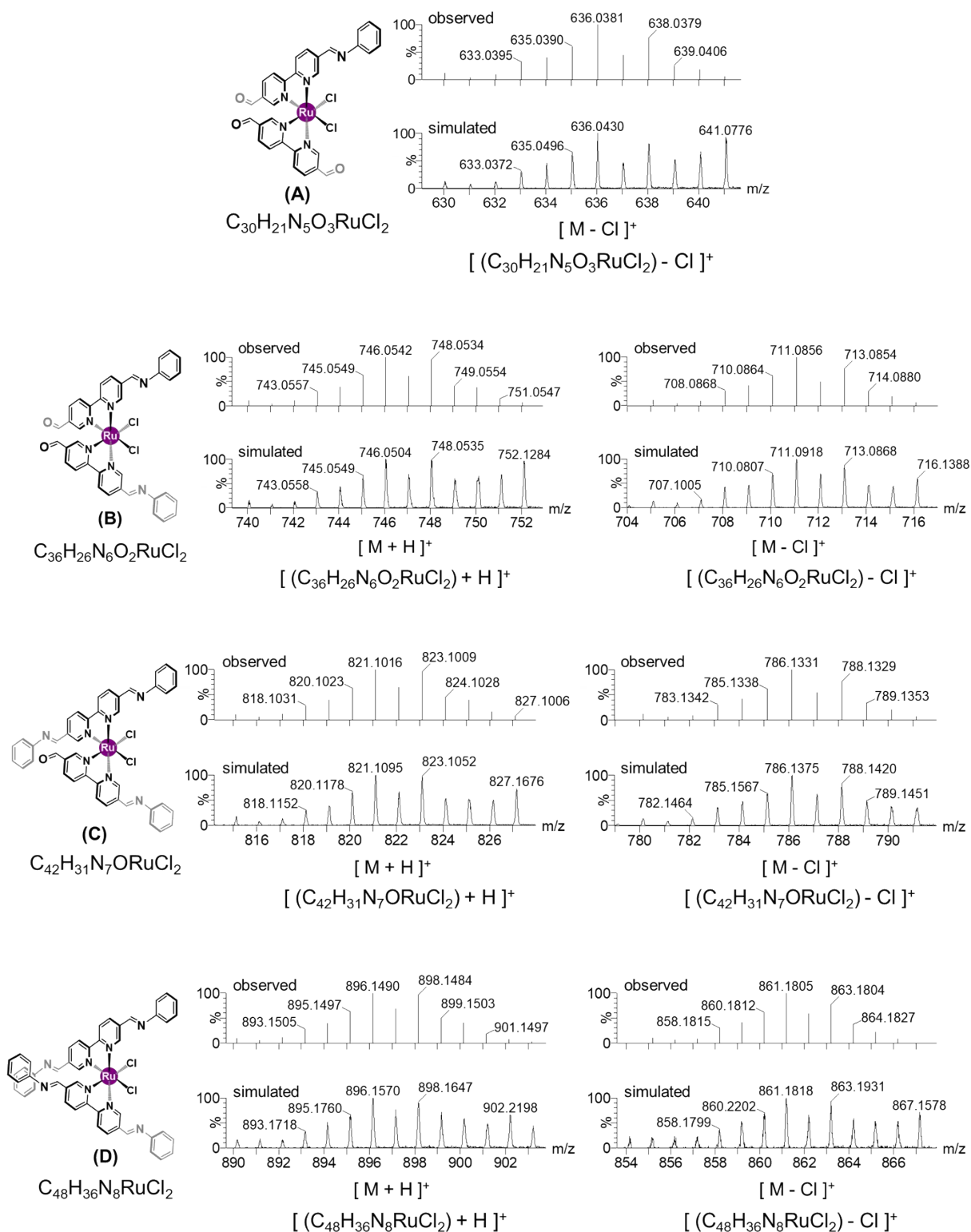


Fig. S8 The observed and simulated isotopic peak distribution showing the corresponding +1 ion peaks.

2.4 X-ray single crystal structure of model compound Ru(bpy-Ph)₂Cl₂

Single-crystal X-ray diffraction data reveals that Ru(bpy-Ph)₂Cl₂ crystallizes in the triclinic *P*-1 space group. The Ru(II) centre is in a typical distorted octahedral geometry. Each Ru(II) coordinate with four nitrogen atoms from two bipyridine derived ligands, another two chloride anions also coordinate with the Ru(II) centre for charge balance. The average Ru-N bond length is 2.040 Å, and the average Ru-Cl bond length is 2.422 Å. The X-ray single crystal structure further proved that the Ru(bpy-CHO)₂Cl₂ building unit is stable in the solvothermal condition for the synthesis of MCOFs. Final crystallographic data for Ru(bpy-Ph)₂Cl₂ is listed in Table S2. CCDC: 2270379.

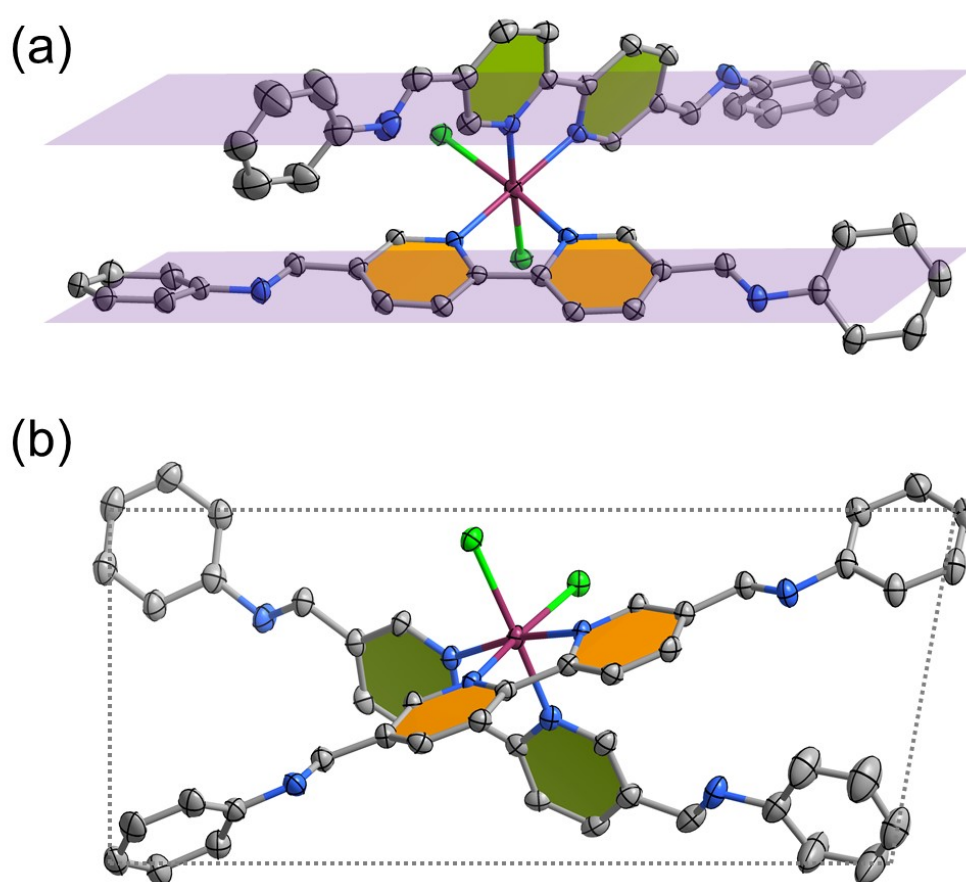


Fig. S9 The single crystal X-ray structure for Ru(bpy-Ph)₂Cl₂ (ORTEP, 30% ellipsoids), which exhibited the similar geometric features with Ru(bpy-CHO)₂Cl₂ linkers. All H atoms and solvent molecules have been removed for clarity (C: Grey; N: blue; Ru: purple)

Table S2 Summary of crystallographic data for Ru(bpy-Ph)₂Cl₂

Ru(bpy-Ph) ₂ Cl ₂	
Formula	C ₁₀₈ H ₁₀₁ Cl ₄ N ₂₀ O ₄ Ru ₂
Formula Weight	2087.02
<i>T</i> (K)	193
λ (Å)	1.34139
Crystal system	triclinic
Space group	<i>P</i> -1
<i>a</i> (Å)	12.1419(5)
<i>b</i> (Å)	14.3036(6)
<i>c</i> (Å)	31.1469(13)
α (°)	83.406(2)
β (°)	80.168(2)
γ (°)	65.193(2)
<i>V</i> (Å ³)	1308.34
<i>Z</i>	2
<i>D</i> _{calc} (Mg/m ³)	1.434
μ (mm ⁻¹)	2.731
<i>F</i> (000)	2154
θ (°)	2.5 - 60.5
Index ranges	-15 ≤ <i>h</i> ≤ 15 -18 ≤ <i>k</i> ≤ 17 -37 ≤ <i>l</i> ≤ 40
Reflections collected	15652
GOF (<i>F</i> ²)	1.040
<i>R</i> _{<i>I</i>} ^a , <i>wR</i> ₂ ^b (<i>I</i> > 2σ(<i>I</i>))	0.0675, 0.1807
<i>R</i> _{<i>I</i>} ^a , <i>wR</i> ₂ ^b (all data)	0.0939, 0.1958

$$R_I^a = \frac{\sum ||F_o| - |F_c||}{\sum F_o} \quad wR_2^b = \frac{[\sum w(F_o^2 - F_c^2)^2 / \sum w(F_o^2)]^{1/2}}{\sum w(F_o^2)^{1/2}}$$

2.5 Synthesis of RuCOFs

The synthesis of RuCOF-100: The RuCOF-100 was synthesized by solvothermal condensation reaction. Ru(bpy-CHO)₂Cl₂ (23.86 mg, 0.04 mmol) and ETTA (15.72 mg, 0.04 mmol) were dissolved in a mixed solvent of 0.5 mL 1,4-dioxane, 0.5 mL mesitylene, 0.2 mL acetonitrile and 0.4 mL 6M aqueous acetic acid in a pyrex tube. This mixture was sonicated for 10 min to get a homogeneous dispersion. Then, the pyrex tube was flash frozen in a liquid N₂ bath and degassed by freeze-pump-thaw technique for three times and sealed under vacuum. Upon warming to room temperature, the tube was placed in an oven and heated at 120 °C for 5 days. The precipitate was collected by filtration, washed with DMF (8 × 5 mL), extracted by soxhlet extractor with tetrahydrofuran for 24 hours, and finally dried at 100 °C under vacuum overnight to obtain reddish-gray crystalline powder. Yield: 68%. Elemental analysis of RuCOF-100: Calcd. for C₂₀₀H₁₂₈N₃₂Cl₈Ru₄: C, 65.50%; H, 3.52%; N, 12.22%. Found: C, 66.23%; H, 3.32%; N, 11.64%.

The synthesis of RuCOF-101: The RuCOF-101 was synthesized by solvothermal condensation reaction. Ru(bpy-CHO)₂Cl₂ (23.86 mg, 0.04 mmol) and ETTBA (27.88 mg, 0.04 mmol) were dissolved in a mixed solvent of 0.2 mL 1,4-dioxane, 0.8 mL mesitylene, 0.2 mL acetonitrile and 0.4 mL 6M aqueous acetic acid in a pyrex tube. This mixture was sonicated for 10 min to get a homogeneous dispersion. Then, the pyrex tube was flash frozen in a liquid N₂ bath and degassed by freeze-pump-thaw technique for three times and sealed under vacuum. Upon warming to room temperature, the tube was placed in an oven and heated at 120 °C for 5 days. The precipitate was collected by filtration, washed with DMF (8 × 5 mL), extracted by soxhlet extractor with tetrahydrofuran for 24 hours, and finally dried at 100 °C under vacuum overnight to obtain brownish green crystalline powder. Yield: 76%. Elemental analysis of RuCOF-101: Calcd. for C₂₉₆H₁₉₂N₃₂Cl₈Ru₄: C, 72.78%; H, 3.96%; N, 9.17%. Found: C, 73.49%; H, 3.25%; N, 9.85%.

The synthesis of RuCOF-100': The mixture of 160.00 mg RuCOF-100 and 100 mg AgNO₃ in a solution of 5mL de-ionized water and 10 mL ethanol was stirred under argon at 50 °C overnight. Then, the precipitate was collected by filtration, washed with DMF (8 × 5 mL) and THF (8 × 5 mL), and finally dried at 60 °C under vacuum overnight to obtain black-gray crystalline powder. Yield: 89%.

The synthesis of RuCOF-101': The mixture of 160 mg RuCOF-101 and 100 mg AgNO₃ in a solution of 5mL de-ionized water and 10 mL ethanol was stirred under argon at 50 °C overnight. Then, the precipitate was collected by filtration, washed with DMF (8 × 5 mL) and THF (8 × 5 mL), and finally dried at 60 °C under vacuum overnight to obtain brown crystalline powder. Yield: 93%.

2.6 FT-IR analysis

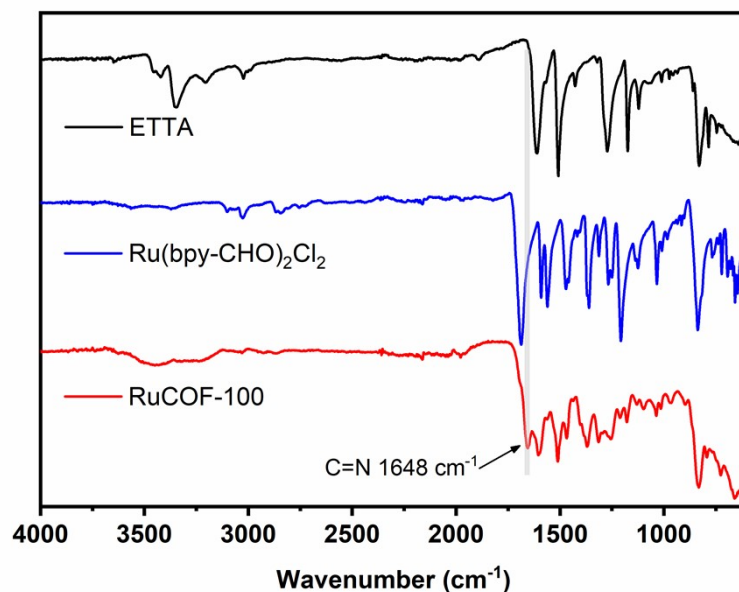


Fig. S10 FT-IR spectra of ETTA, Ru(bpy-CHO)₂Cl₂ and RuCOF-100.

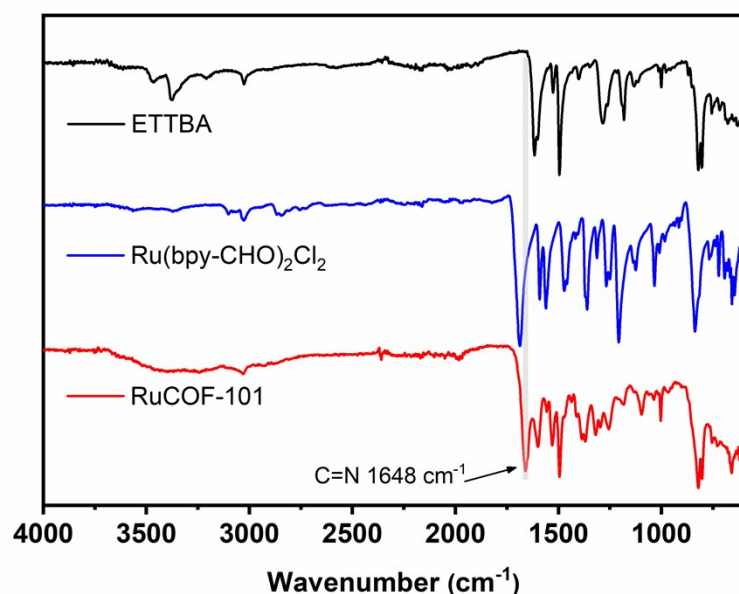


Fig. S11 FT-IR spectra of ETTBA, Ru(bpy-CHO)₂Cl₂ and RuCOF-101.

The as-synthesized materials were characterized by FT-IR. Compared with the building units, the C=O (1690 cm⁻¹) from Ru(bpy-CHO)₂Cl₂ segments and N-H stretching vibrations (3250-3450 cm⁻¹) from amines were disappeared for RuCOFs. Meanwhile, the characteristic C=N stretching vibration was appeared at around 1648 cm⁻¹, which clearly suggested the formation of imine linkages.

2.7 Solid-state ^{13}C NMR spectra

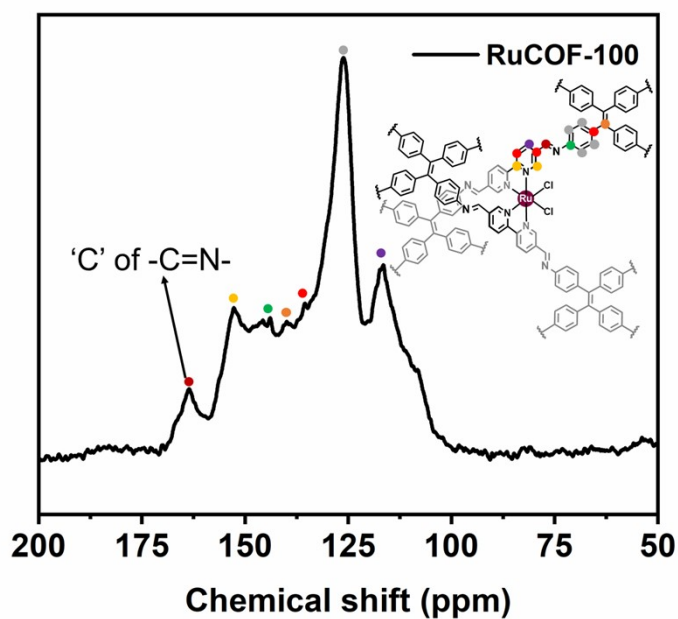


Fig. S12 ^{13}C solid-state NMR spectrum of RuCOF-100.

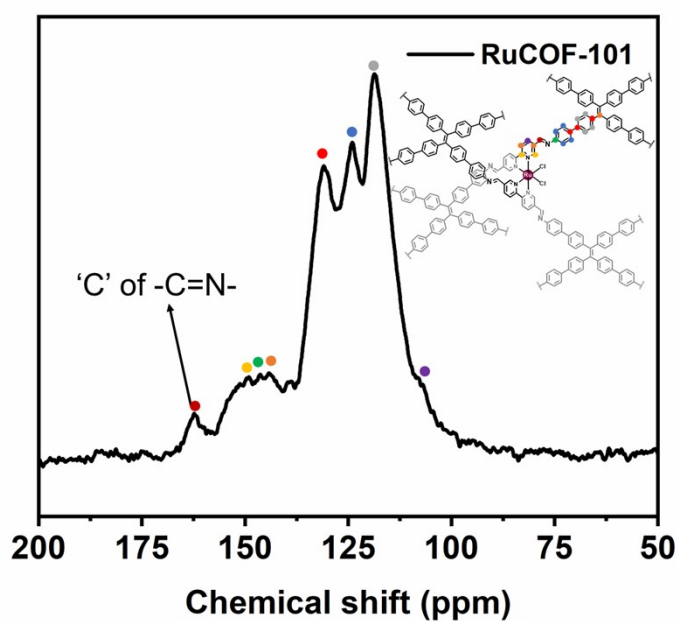


Fig. S13 ^{13}C solid-state NMR spectrum of RuCOF-101.

The as-synthesized materials were characterized by ^{13}C solid-state NMR spectra. The appearance of characteristic resonance peak of imine carbon (162 ppm for RuCOF-100 and 161 ppm for RuCOF-101) suggested the successful formation of imine linkage. Besides, the signals of benzene and bipyridine unit appeared between 160 and 100 ppm.

2.8 Chemical stability

The as-synthesized RuCOF-100 and RuCOF-101 powders (20 mg) were immersed in different solvents at room temperature for 48 hours, respectively. The powders were then separated by centrifugation and washed with tetrahydrofuran three times, and dried in a 50 °C vacuum oven for 6 hours. Then, the powders were used for the FT-IR and PXRD measurements. As shown in the following, both of the as-synthesized RuCOFs are stable in all the solutions.

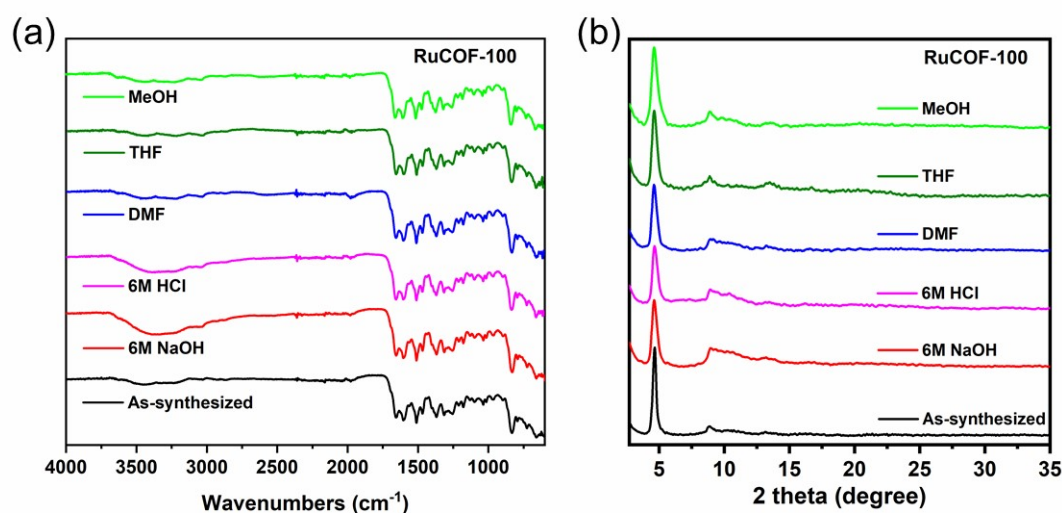


Fig. S14 (a) FT-IR spectra and (b) PXRD patterns of RuCOF-100 before and after immersion in different solvents.

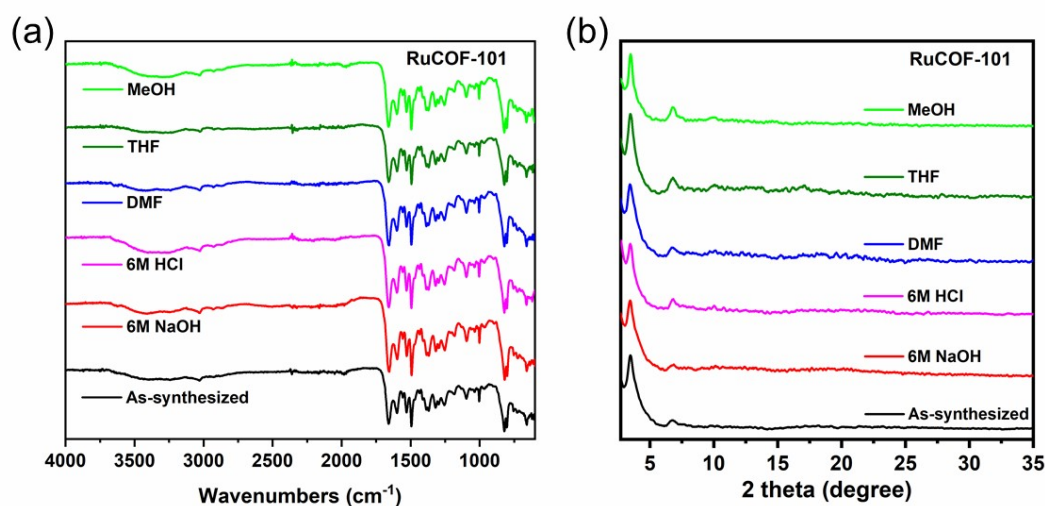


Fig. S15 (a) FT-IR spectra and (b) PXRD patterns of RuCOF-101 before and after immersion in different solvents.

2.9 Thermogravimetric analysis

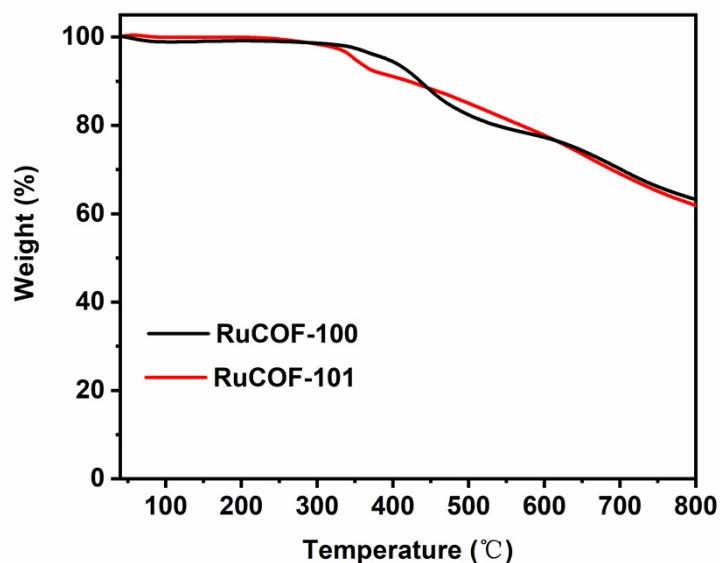


Fig. S16 TGA profiles of RuCOF-100 (black) and RuCOF-101 (red).

The two RuCOFs showed similar thermal stability. Upon heating to 350 °C, there were only a slight loss of weight (less than 5%). With further heating to 800 °C, there were still more than 60% of the initial mass retaining for both of the RuCOFs.

2.10 High resolution transmission electron microscopy (HRTEM)

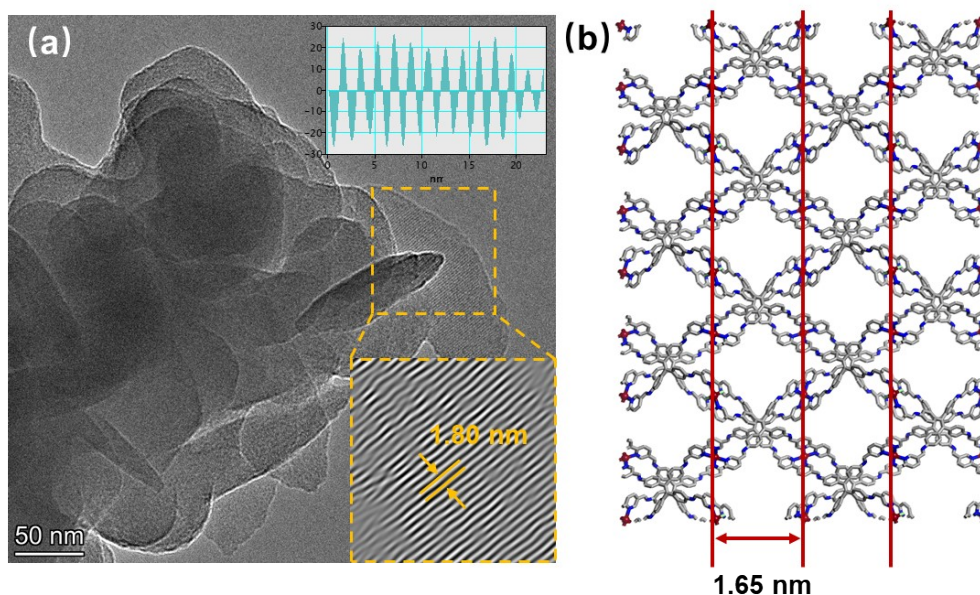


Fig. S17 (a) HRTEM image of RuCOF-100. Insets: Fourier-filtered image of the selected region showing the d -spacing value of 1.80 nm. (b) The structural model of RuCOF-100 in a '2x2x2' unit takes along the [001] direction. All H atoms have been removed for clarity (C: Grey; N: blue; Ru: purple).

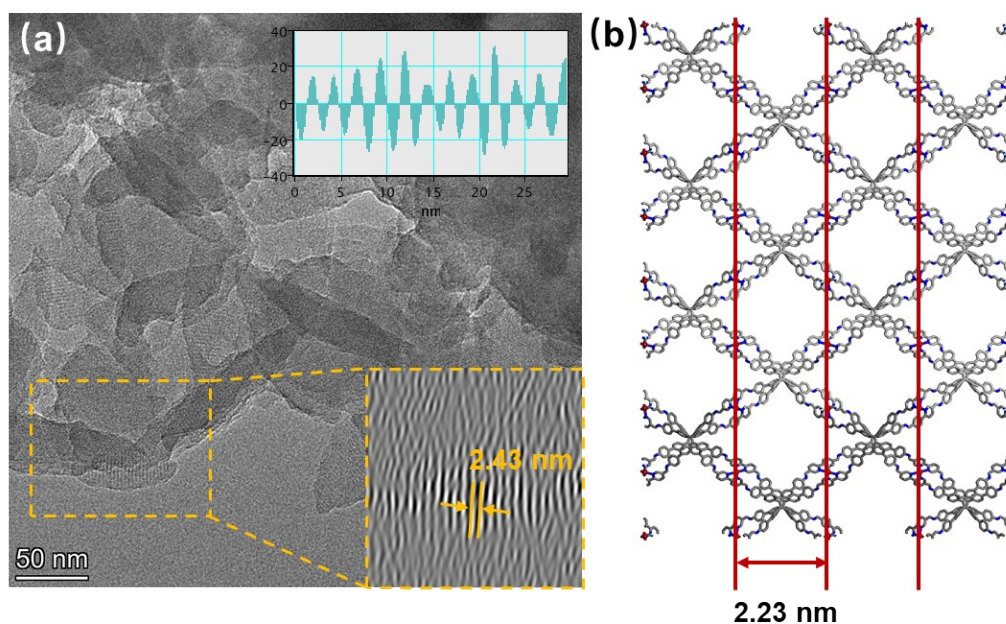


Fig. S18 (a) HRTEM image of RuCOF-101. Insets: Fourier-filtered image of the selected region showing the d -spacing value of 2.43 nm. (b) The structural model of RuCOF-101 in a '2×2×2' unit takes along the [001] direction. All H atoms have been removed for clarity (C: Grey; N: blue; Ru: purple).

The HRTEM images with clear lattice fringes demonstrated the crystalline structure of the as-synthesized RuCOFs. For RuCOF-100, the d -spacing value was 1.80 nm, which was close to the theoretical distance between Ru-to-Ru in our proposed structure taking along the [001] direction (Fig. S17). For RuCOF-101, the d -spacing value of 2.43 nm was also observed in the HRTEM image, which agreed with the theoretical distance (2.23 nm) of the [001] plane as well (Fig. S18). These results further confirmed the rationality of the simulated structures.

2.11 XPS analysis

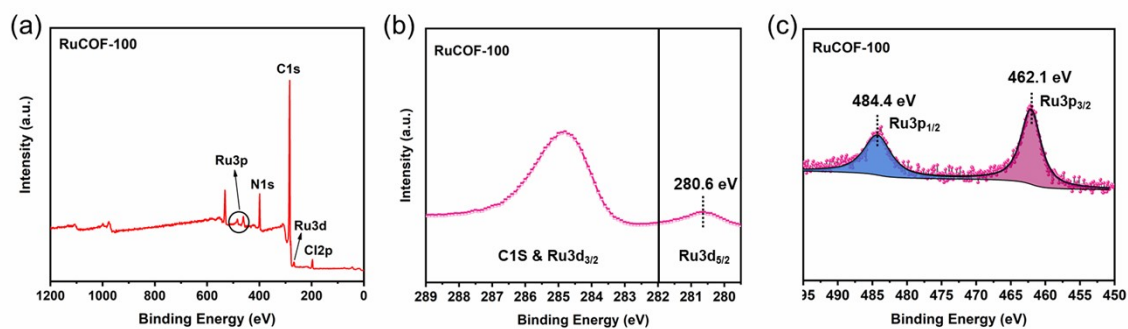


Fig. S19 (a) XPS survey spectrum of RuCOF-100. The comparison of the high-resolution XPS spectra of RuCOF-100 for region (b) Ru 3d/C 1s and (c) Ru 3p, respectively.

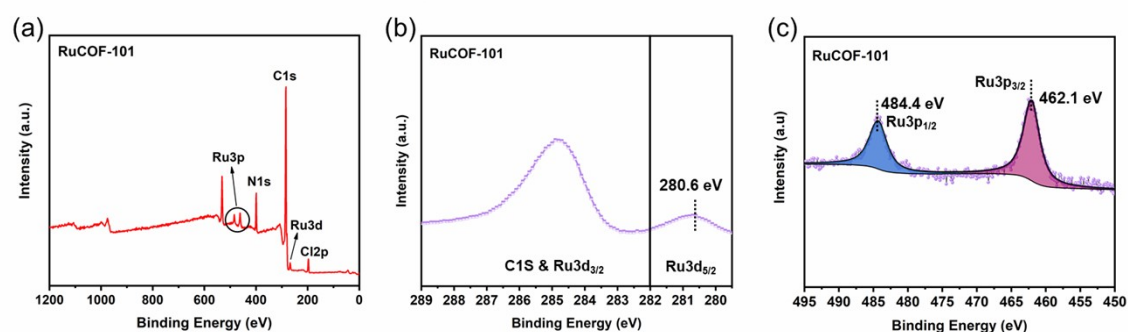


Fig. S20 (a) XPS survey spectrum of RuCOF-101. The comparison of the high-resolution XPS spectra of RuCOF-101 for region (b) Ru 3d/C 1s and (c) Ru 3p, respectively.

To understand the surface elemental composition and chemical states, XPS measurements were conducted. The experimental results supported the composition of C, N, Ru and Cl elements for the RuCOF-100 and RuCOF-101.

Section 3. PXRD analysis and structural modeling of the RuCOFs

3.1 Comparison of PXRD patterns for RuCOFs and their related monomers

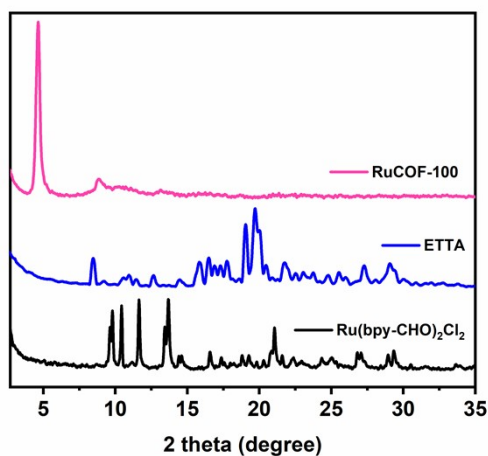


Fig. S21 The comparison of experimental PXRD patterns for RuCOF-100 and its starting materials, ETTA and Ru(bpy-CHO)₂Cl₂. The RuCOF-100 shows distinct reflections with respect to both starting materials.

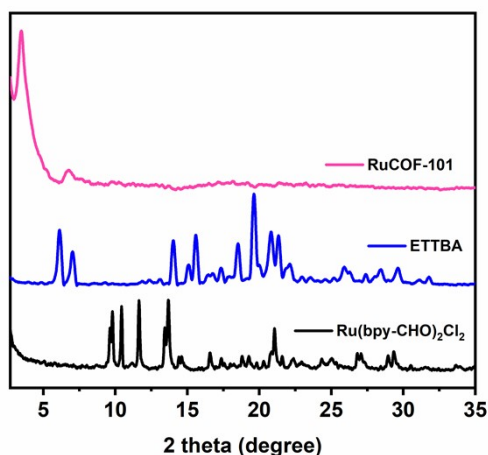


Fig. S22 The comparison of experimental PXRD patterns for RuCOF-101 and its monomers, ETTBA and Ru(bpy-CHO)₂Cl₂. The RuCOF-101 shows distinct reflections with respect to both starting materials.

3.2 Structural modeling of the RuCOFs

Molecular modeling was conducted with the Materials Studio (ver. 8.0) program. Considering the geometry of the precursors and the connection patterns, we constructed models for each of the possible structures (eg. 2D **sql** net, and 3D **lvt**, **ssb** nets), and compared their simulated PXRD patterns with the experimental data. The vertex positions were obtained from Reticular Chemistry Structure Resource (RCSR) database for structural modeling. The structural models were geometrically optimized using MS Forcite molecular dynamics

module method. Pawley refinement was carried out using Reflex software package. The Pawley refinements were performed to optimize the lattice parameters iteratively until the R_p and R_{wp} value converges and the overlay of the observed with refined profiles showed good agreement. Rietveld refinements were also carried out using the GSAS-II software package with a general least squares fit.

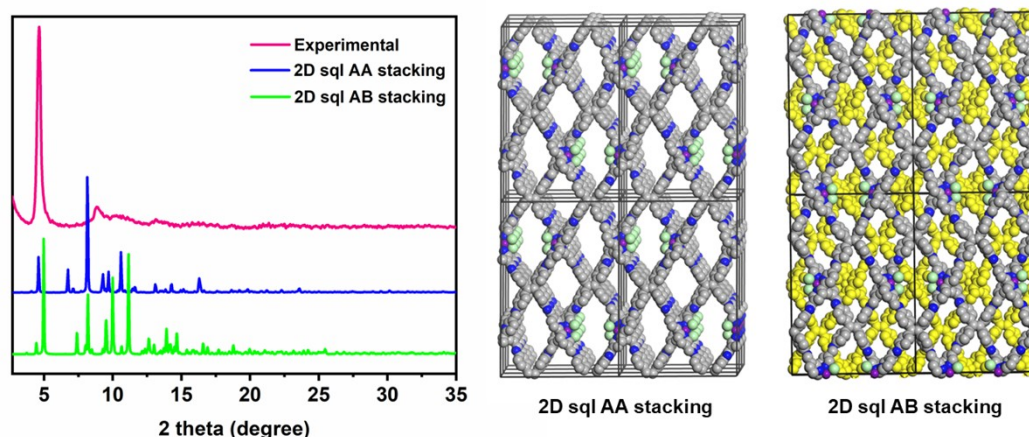


Fig. S23 The comparison of experimental and simulated PXRD patterns of RuCOF-100, where the structural models were constructed based on **sql** net with AA and AB stacking, respectively. AA stacking: space group $P2/c$, $a = 9.73 \text{ \AA}$, $b = 26.23 \text{ \AA}$, $c = 39.25 \text{ \AA}$, $\alpha = 90^\circ$, $\beta = 102.34^\circ$, $\gamma = 90^\circ$. AB stacking: space group $P2$, $a = 14.40 \text{ \AA}$, $b = 26.28 \text{ \AA}$, $c = 39.10 \text{ \AA}$, $\alpha = 90^\circ$, $\beta = 101.98^\circ$, $\gamma = 90^\circ$.

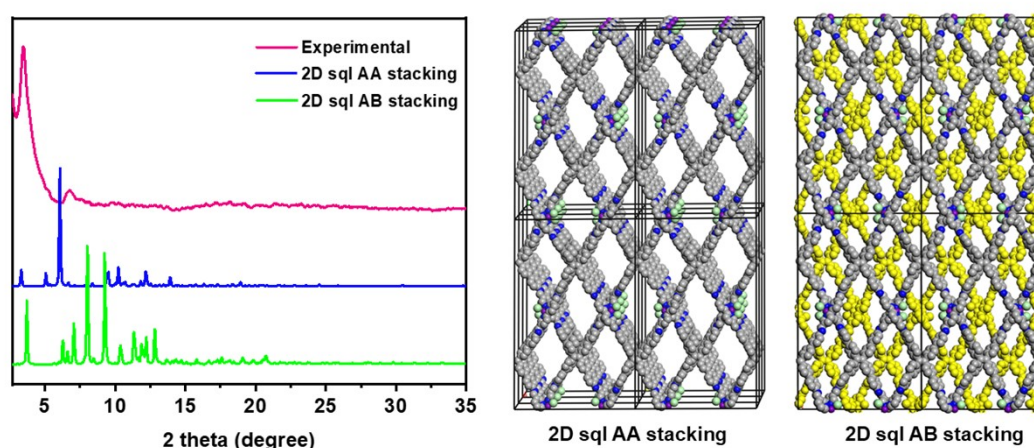


Fig. S24 The comparison of experimental and simulated PXRD patterns of RuCOF-101, where the structural models were constructed based on **sql** net with AA and AB stacking, respectively. AA stacking: space group $P2$, $a = 9.62 \text{ \AA}$, $b = 34.64 \text{ \AA}$, $c = 54.25 \text{ \AA}$, $\alpha = 90^\circ$, $\beta = 102.99^\circ$, $\gamma = 90^\circ$. AB stacking: space group $P2$, $a = 16.65 \text{ \AA}$, $b = 33.31 \text{ \AA}$, $c = 54.89 \text{ \AA}$, $\alpha = 90^\circ$, $\beta = 106.18^\circ$, $\gamma = 90^\circ$.

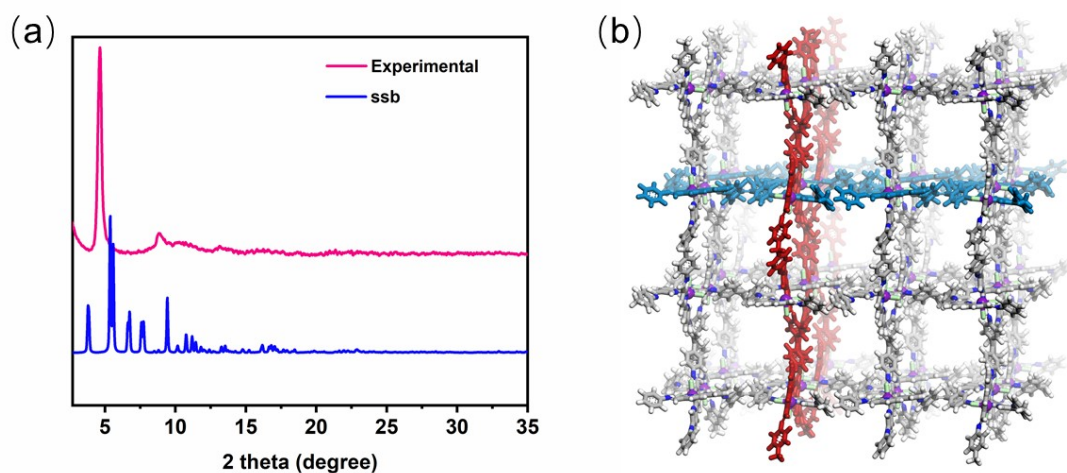


Fig. S25 Simulated PXRD pattern and structure of RuCOF-100 with **ssb** topology. (a) experimental (red) and simulated PXRD patterns (blue). (b) The corresponding structure of **ssb** net built from ETTA and Ru(bpy-CHO)₂Cl₂, where two interlocked 2D grids from different orientations were represented by different colors (red and blue) for clarity. Space group *I222*, $a = 31.60 \text{ \AA}$, $b = 33.00 \text{ \AA}$, $c = 32.83 \text{ \AA}$, $\alpha = \beta = \gamma = 90^\circ$.

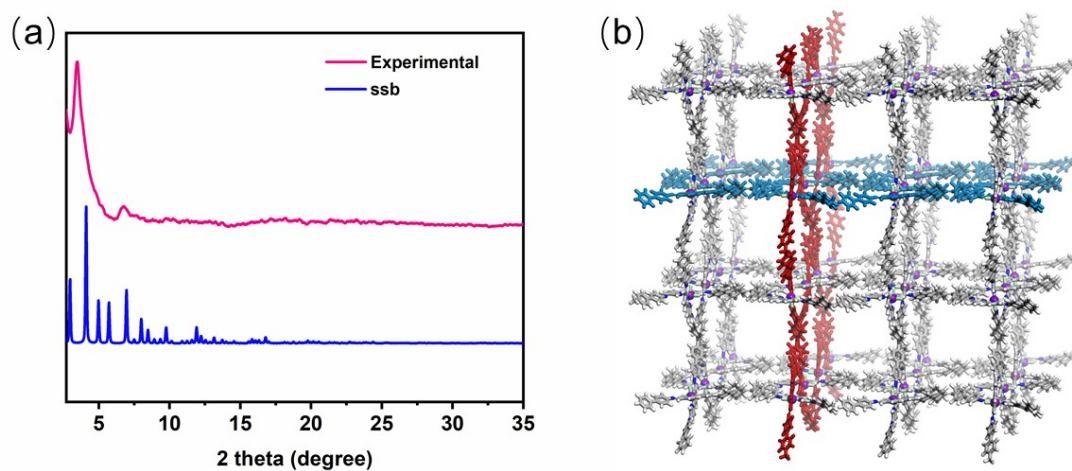


Fig. S26 Simulated PXRD pattern and structure of RuCOF-101 with **ssb** topology. (a) experimental (red) and simulated PXRD patterns (blue). (b) The corresponding structure of **ssb** net built from ETTBA and Ru(bpy-CHO)₂Cl₂, where two interlocked 2D grids from different orientations were represented by different colors (red and blue) for clarity. Space group *I222*, $a = b = c = 45.07 \text{ \AA}$, $\alpha = \beta = \gamma = 90^\circ$.

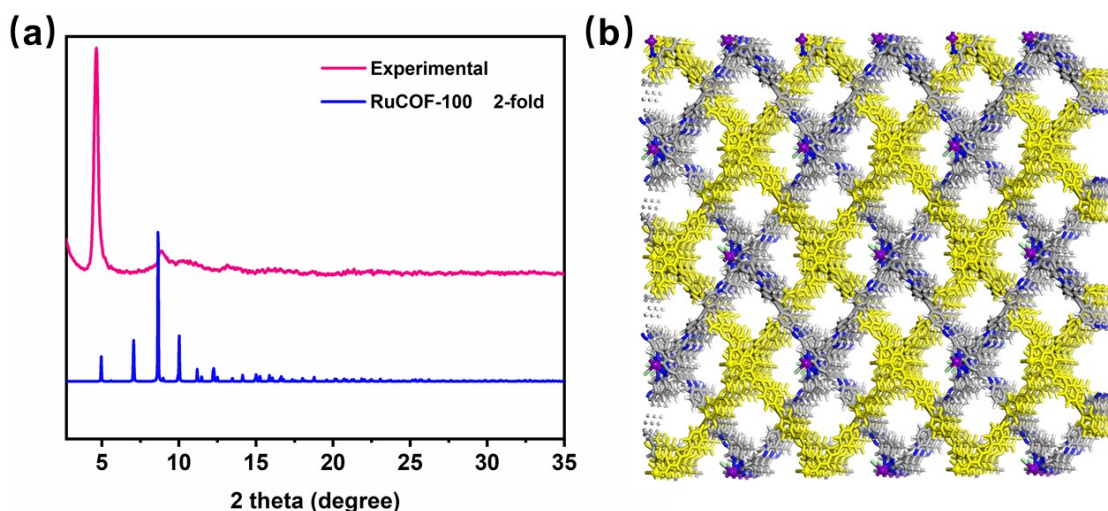


Fig. S27 Simulated PXRD pattern and structure of RuCOF-100 with 2-fold interpenetrated **lvt** topology. (a) Experimental (red) and simulated PXRD patterns (blue). (b) The corresponding structure of RuCOF-100 with 2-fold interpenetrated **lvt** nets. Space group *Pnc2*, $a = 24.96 \text{ \AA}$, $b = 35.55 \text{ \AA}$, $c = 24.93 \text{ \AA}$, $\alpha = \beta = \gamma = 90^\circ$.

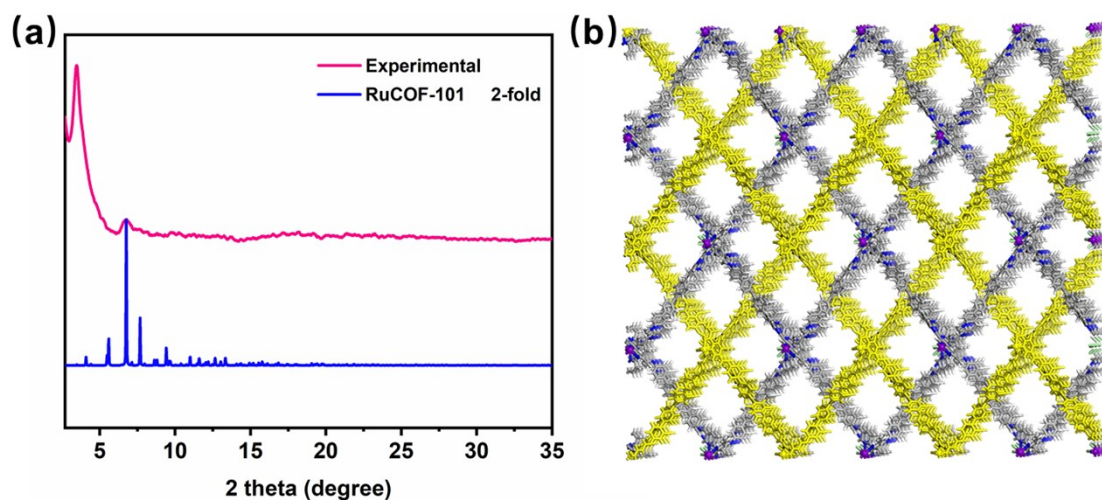


Fig. S28 Simulated PXRD pattern and structure of RuCOF-101 with 2-fold interpenetrated **lvt** topology. (a) Experimental (red) and simulated PXRD patterns (blue). (b) The corresponding structure of RuCOF-101 with 2-fold interpenetrated **lvt** nets. Space group *Pnc2*, $a = 33.20 \text{ \AA}$, $b = 45.21 \text{ \AA}$, $c = 33.30 \text{ \AA}$, $\alpha = \beta = \gamma = 90^\circ$.

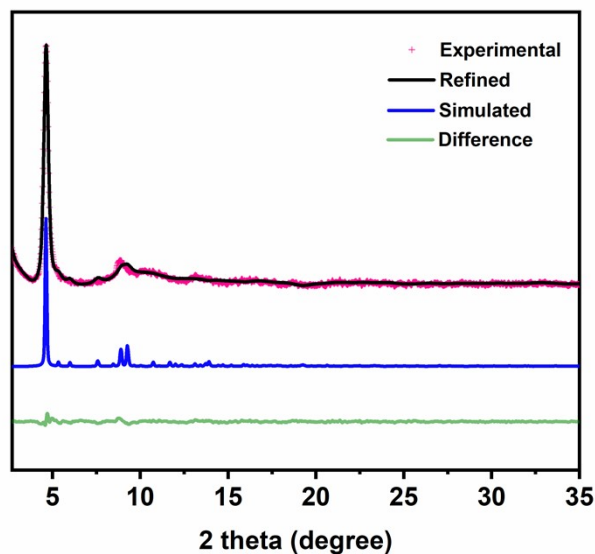


Fig. S29 The experimental (red), Rietveld refined (black), the difference (green) and simulated PXRD patterns (blue) of RuCOF-100. Space group $P-4$, $a = 23.14 \text{ \AA}$, $b = 33.06 \text{ \AA}$, $c = 23.38 \text{ \AA}$, $\alpha = \beta = \gamma = 90^\circ$, $wR = 2.749$, Reduced $\chi^2 = 0.39$.

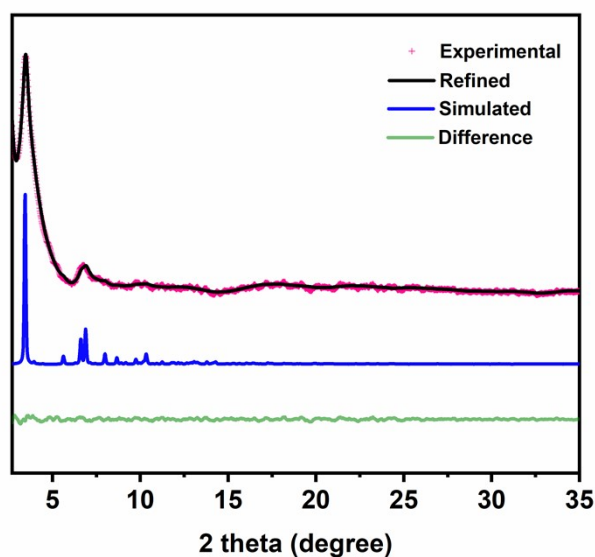


Fig. S30 The experimental (red), Rietveld refined (black), the difference (green) and the simulated (blue) PXRD patterns of RuCOF-101. Space group $P-4$, $a = 31.17 \text{ \AA}$, $b = 44.65 \text{ \AA}$, $c = 31.35 \text{ \AA}$, $\alpha = \beta = \gamma = 90^\circ$, $wR = 2.544$, Reduced $\chi^2 = 0.21$.

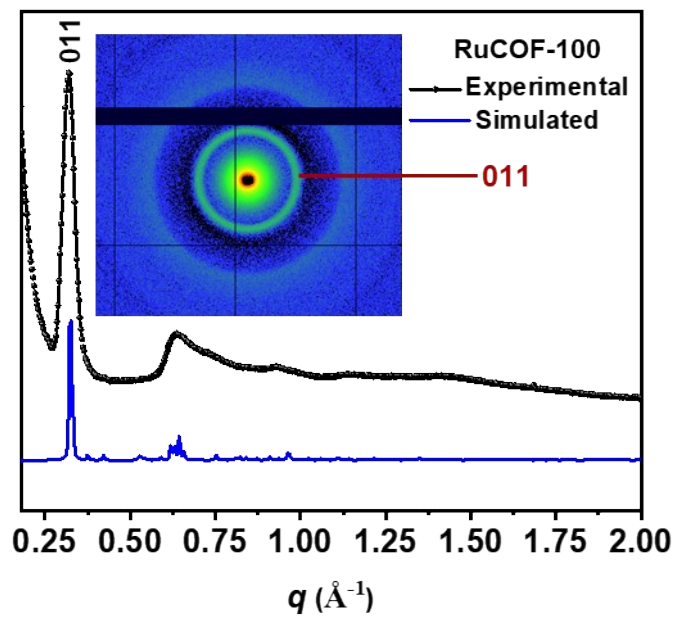


Fig. S31 The 1D SAXS plots of RuCOF-100, in which the insets show 2D SAXS image.

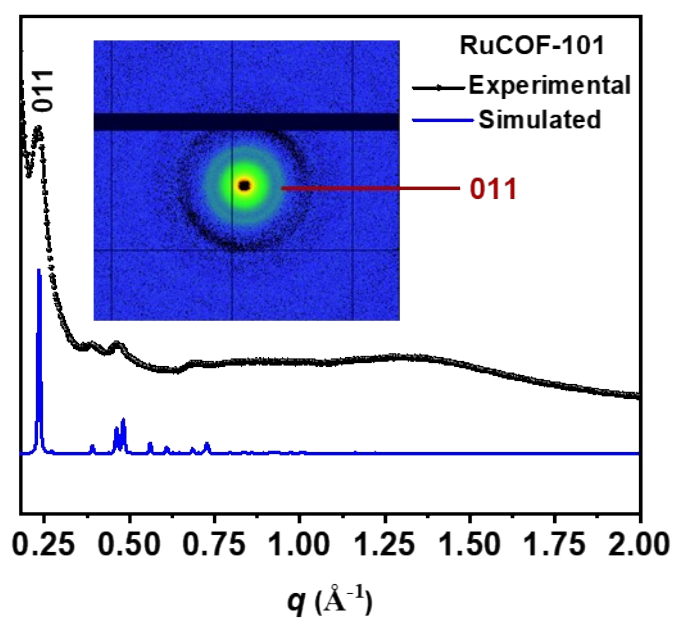


Fig. S32 The 1D SAXS plots of RuCOF-101, in which the insets show 2D SAXS image.

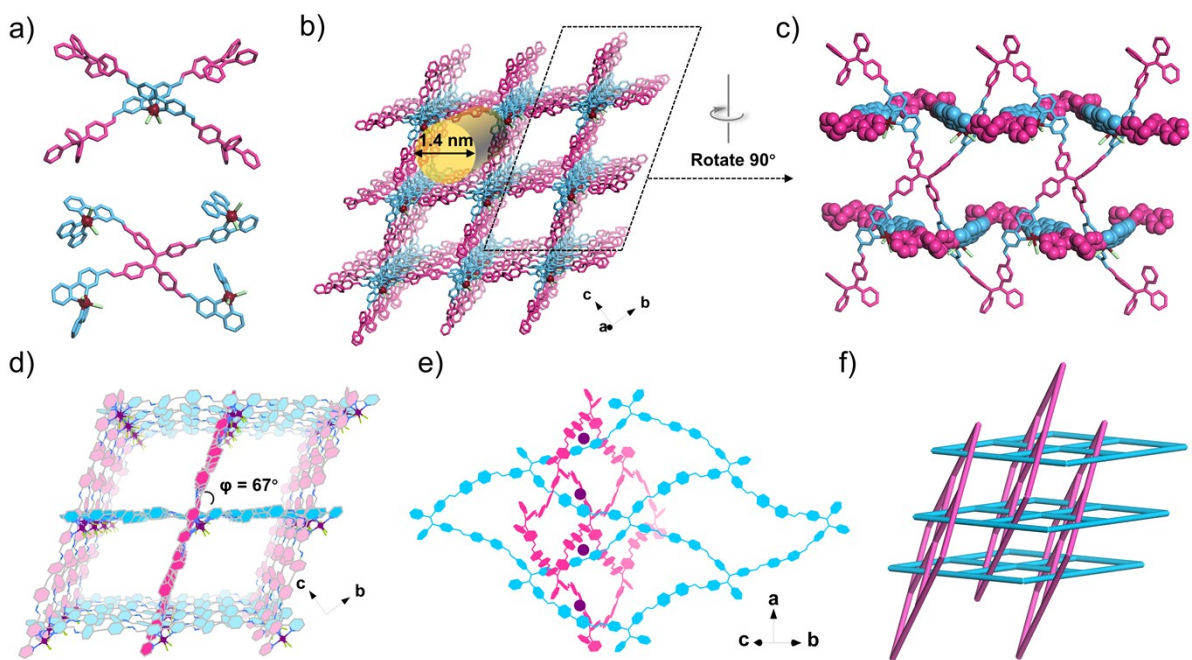


Fig. S33 The structure of RuCOF-100: (a) Linking Ru(bpy-CHO)₂Cl₂ and ETDA with 4,4-connected pattern, (b) affording the formation of a 3D framework. (c) Views showing the inclined interpenetration of the covalent components. (d) Overall 3D framework shows the interlocking of 2D networks, where the 2D network are represented in green and pink, respectively. (e) Structural representation of two 2D **sql** layers threaded through the wide opening of the rhombic windows with the Ru(II) ions as templates. (f) the corresponding 3D topology, highlighting the interdigitation of 2D networks.

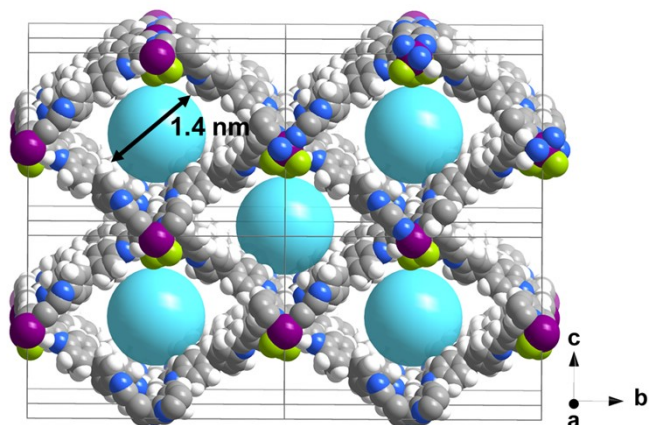


Fig. S34 Theoretical pore size of RuCOF-100, showing the structure in a '2×2×2' cells. C, gray; N, blue; Ru, purple; Cl, green; H, white.

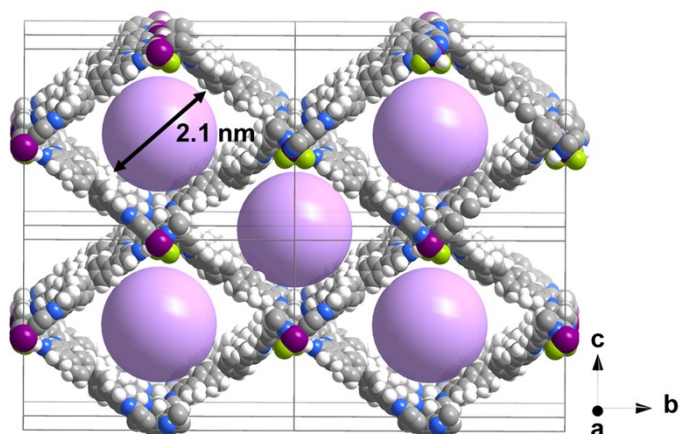


Fig. S35 Theoretical pore size of RuCOF-101, showing the structure in a '2×2×2' cells. C, gray; N, blue; Ru, purple; Cl, green; H, white.

3.3 PXRD analysis of the RuCOFs with substituting the Cl ligands

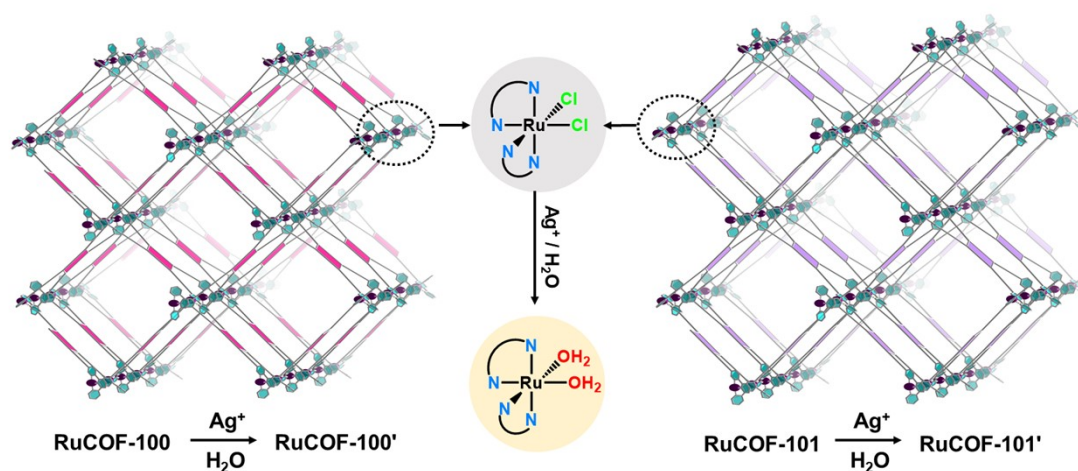


Fig. S36 The synthesis of RuCOF-100' and RuCOF-101' by substituting the Cl ligands of RuCOF-100 and RuCOF-101, respectively.

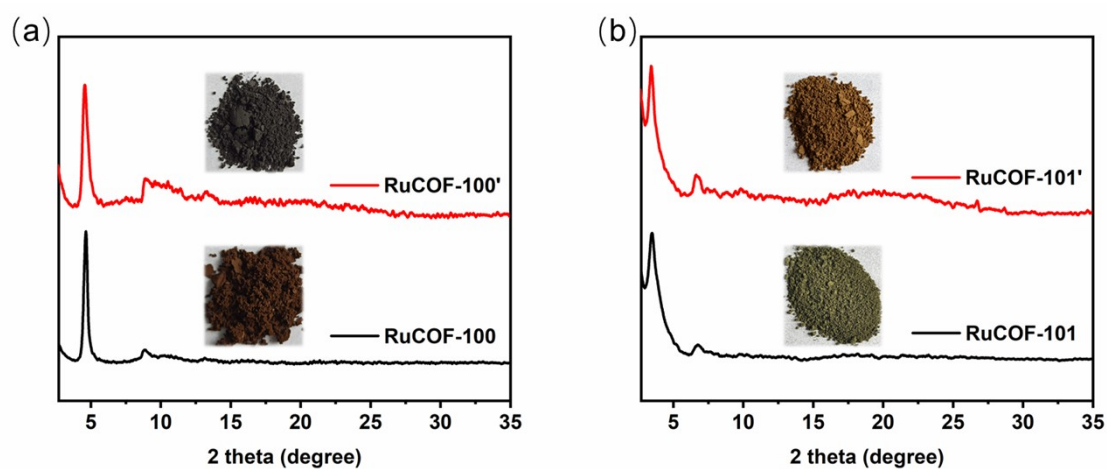


Fig. S37 The comparison of PXRD patterns of RuCOF-100 and RuCOF-100', RuCOF-101 and RuCOF-101', respectively, confirming the retention of crystallinity after the substitution of Cl ligands. Insets: the powder samples of corresponding RuCOFs.

Section 4. Water oxidation experiments

4.1 Oxygen evolution measurements

Oxygen measurements were performed with a calibrated O₂ electrode (JPBJ-608). Calibration was performed by measuring signal in oxygen-saturated deionized water and freshly prepared oxygen-depleted reagent (5% Na₂SO₃ solution), respectively.

(a) Chemically driven water oxidation: the reactions were performed at ambient condition in a 25 ml air-tight quartz reaction vessel. For each standard measurement, an appropriate amount of RuCOF catalyst was dispersed in 18 mL deionized water at pH = 1 (trifluoromethane sulfonic acid was used to adjust the pH value). The resulting mixture was ultrasonicated for 30 mins to get a uniformly dispersed suspension, and then purged with high-purity Ar until the digital readout stabilized. Then, 1.82 mmol of Cerium(IV) ammonium nitrate (CAN) in 2 mL deoxygenated aqueous solution (pH = 1) was injected. O₂ evolution *vs* time was recorded. During the measurement, the reaction temperature was maintained at 25 °C using a condenser, and the stirring speed was kept at 200 rpm.

(b) Photocatalytic water oxidation: the reactions were carried out in a 25 mL air-tight quartz reaction vessel. For each standard measurement, an appropriate amount of RuCOF catalyst was dispersed in 20 mL 3:7 CH₃CN/aqueous phosphate buffer solution (pH = 7) containing [Ru(bpy)₃]Cl₂ (1.5 mM) and Na₂S₂O₈ (37 mM) in the dark. The resulting mixture was ultrasonicated for 30 mins to get a uniformly dispersed suspension, and then purged with high-purity Ar until the digital readout stabilized. The sample was then irradiated under a 300 W Xe lamp with a 420 nm cutoff filter to imitate visible light irradiation (420 nm ≤ λ ≤ 780 nm). O₂ evolution *vs* time was recorded. During the measurement, the reaction temperature was maintained at 25 °C using a condenser, and the stirring speed was kept at 200 rpm.

4.2 Water contact angle tests

Contact angles measurements of the MCOFs before and after the Cl removal were carried out to evaluate their water wettability. Water wettability generally matters during catalytic oxygen evolution because it is vital to afford excellent catalyst dispersibility and favorable interaction with water. The water contact angles of RuCOF-100 and RuCOF-101 were evaluated to be 55.43° and 46.97° (Fig. S38 a-b), respectively. In comparison, the water contact angles of RuCOF-100' and RuCOF-101' were decreased to 40.32° and 35.35° (Fig. S38 c-d), respectively, indicating their enhanced hydrophilicity for promoting well dispersibility in water after the Cl ligands removal. Meanwhile, two water molecules would coordinate with one Ru(II) center (Fig. S36), in such way, the coordinated water molecules could be accelerated oxidation by the active Ru center.

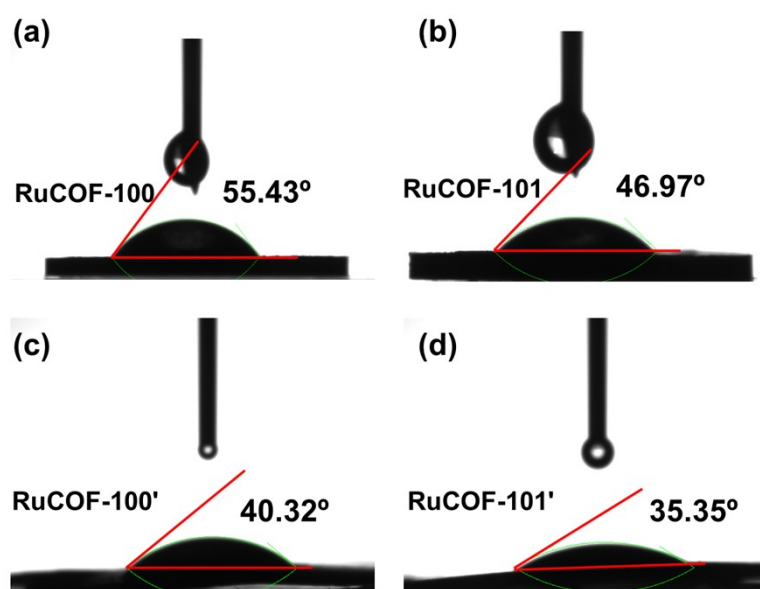


Fig. S38 Water contact angle measurements of (a) RuCOF-100, (b) RuCOF-101, (c) RuCOF-100' and (d) RuCOF-101' at room temperature in air.

4.3 Water oxidation performance

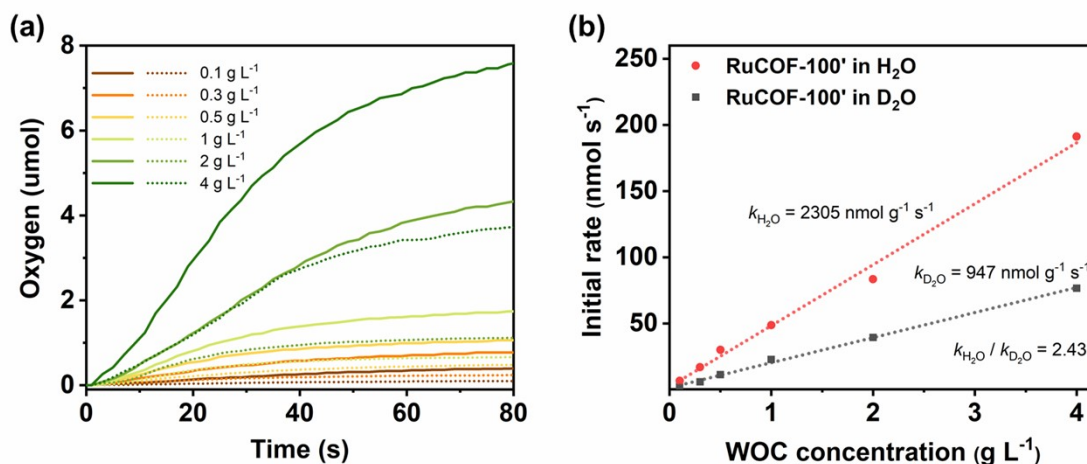


Fig. S39 The kinetic isotope effect experiments for RuCOF-100'. (a) time-dependent oxygen evolution with varying catalyst concentrations in 20 mL aqueous pH = 1 solution (H₂O: solid lines, D₂O: dashed lines); (b) plot of initial catalytic rates (obtained by linear fitting between 10 and 25 s of oxygen evolution curve) versus RuCOFs concentration with corresponding linear regression fit.

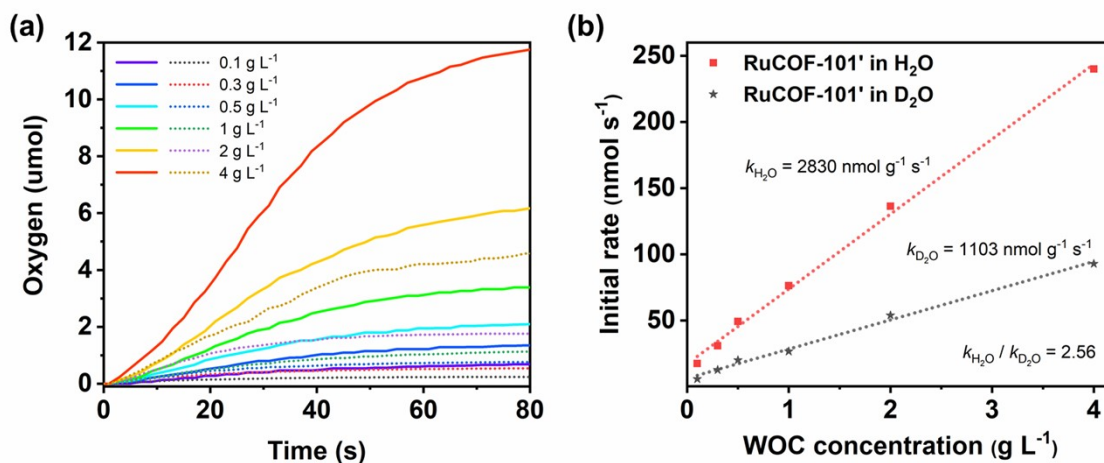


Fig. S40 The kinetic isotope effect experiments for RuCOF-101'. (a) time-dependent oxygen evolution with varying catalyst concentrations in 20 mL aqueous pH = 1 solution (H₂O: solid lines, D₂O: dashed lines); (b) plot of initial catalytic rates (obtained by linear fitting between 10 and 25 s of oxygen evolution curve) versus RuCOFs concentration with corresponding linear regression fit.

TOF calculations

Turnover frequency (TOF) is defined as moles of produced product per mole of catalyst per s^{-1} . The TOF was calculated based on the WOC concentration dependent experiments. The individual initial catalytic rates at each catalyst concentration was determined by linear regression fit of oxygen evolution curve. And the reported TOF was determined from the slope of the plot of the initial rates versus catalyst amount (for the calculation of TOF, the catalyst amount is referred to the amount of Ru active site). Therefore, the calculation of the catalyst amount was estimated as following:

For RuCOF-100', one unit cell with the molecular formula of $C_{200}H_{144}N_{32}O_8Ru_4$ containing four active sites was used. For RuCOF-101', one unit cell with the molecular formula of $C_{296}H_{208}N_{32}O_8Ru_4$ containing four active sites was used.

$$\begin{aligned} TOF (s^{-1}) &= \frac{\text{moles of } O_2 \text{ evolution}}{(\text{moles of catalyst amount}) \times \text{time (s)}} \\ &= \frac{\text{moles of } O_2 \text{ evolution} / \text{time (s)}}{\text{moles of catalyst amount}} \\ &= \frac{\text{catalytic rate}}{\text{moles of catalyst amount}} \end{aligned}$$

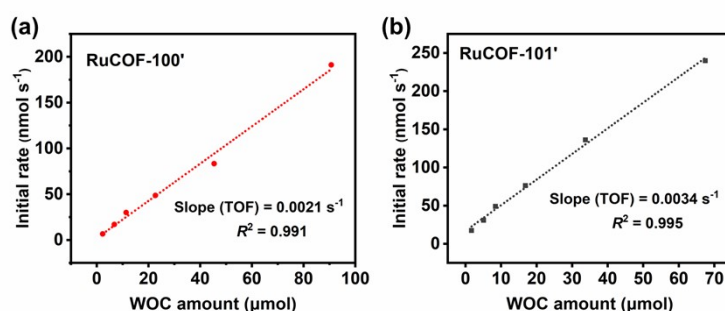


Fig. S41 Chemical water oxidation catalysis: Plot of initial catalytic rates (obtained by linear fitting between 10 and 25 s of oxygen evolution curve) versus the amount of MCOFs active sites with corresponding linear regression fit. The TOF was determined from the slope.

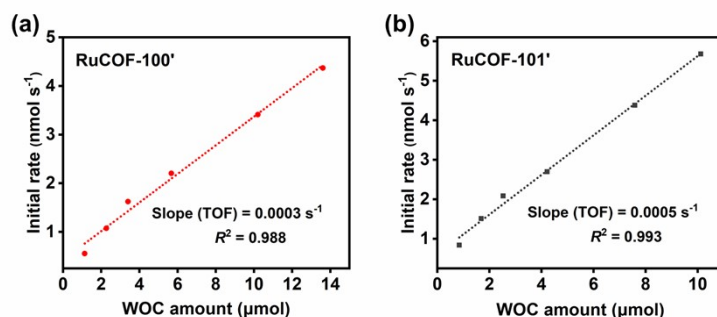


Fig. S42 Photocatalytic water oxidation: Plot of initial catalytic rates (obtained by linear fitting between 90 and 110 s of oxygen evolution curve) versus the amount of MCOFs active sites with corresponding linear regression fit. The TOF was determined from the slope.

Table S3. The comparison of O₂ evolution activity of the as-synthesized MCOFs with Ru-based molecular catalysts.

Catalyst	TOF (s ⁻¹) ^a	References
RuCOF-100'	0.0021	This work
RuCOF-101'	0.0034	
[(bpy) ₂ (OH ₂)Ru–O–Ru(OH ₂)(bpy) ₂](ClO ₄) ₄	0.0042	6
[Ru(tpy)(bpy)(OH ₂)](ClO ₄) ₂	0.0005	7
[Ru(tpy)(bpy-OMe)(OH ₂)](ClO ₄) ₂	0.0011	7
<i>trans, fac</i> -{[Ru(bpea)(H ₂ O)] ₂ (m-bpp)}(PF ₆) ₃	0.0033	8
<i>trans</i> -{[Ru(tpym)(H ₂ O)] ₂ (m-bpp)}(PF ₆) ₃	0.031	8
Ru ₂ (bpp)(tpy) ₂ (H ₂ O) ₂ (PF ₆) ₃	0.014	9
[Ru(bpc)(bpy)OH ₂]PF ₆	0.165	10
Ru(pda)(py) ₂	0.092	11
Ru(pda)(pic) ₂	0.102	11
Ru(bda)(pic) ₂	4.5	11
[Ru(bda)bpb] ₃	150	12
Ru(bda)(isoq) ₂	303	13
MC3@CNT	3200 ^b	14

^aTurnover frequency (TOF) is defined as moles of produced product per mole of catalyst per s⁻¹, in which the per mole of catalyst is referred to the per active site. ^bElectrochemical water oxidation.

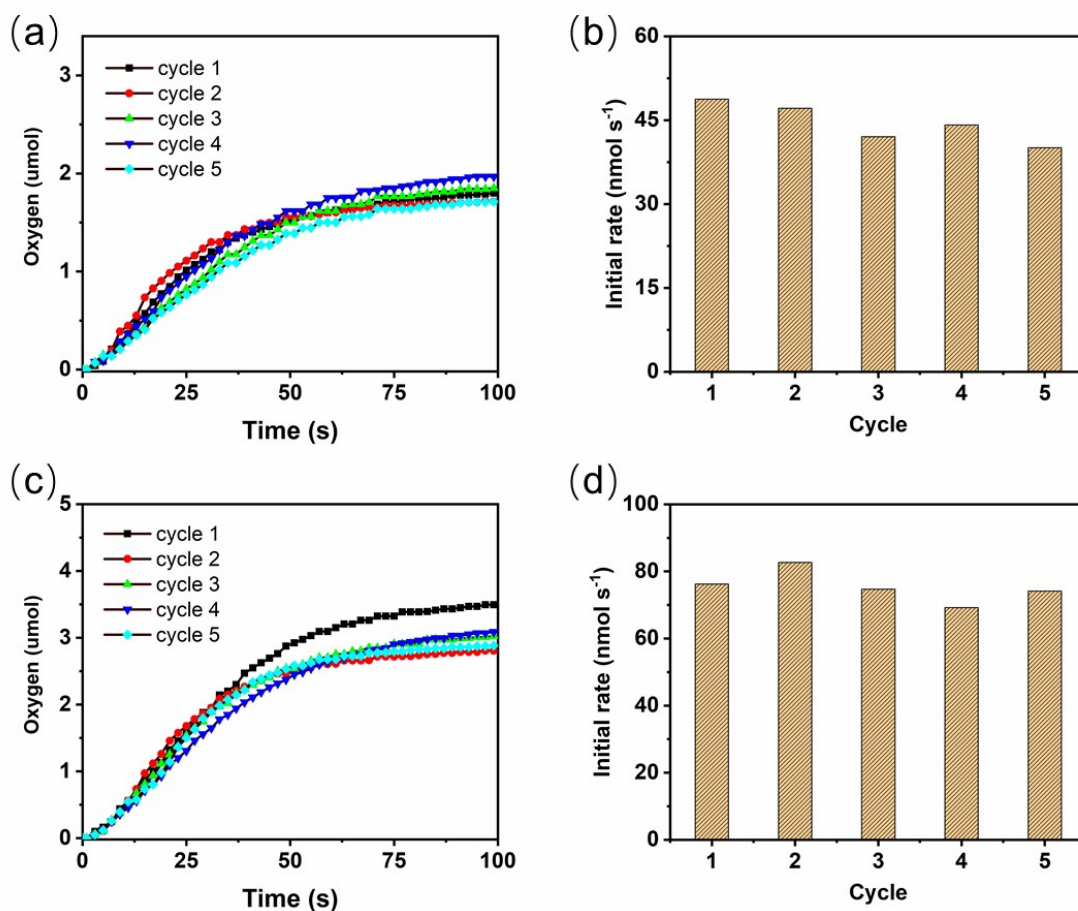


Fig. S43 The recyclability of chemical water oxidation (WOC concentration 1 g L⁻¹): The time-dependent oxygen evolution of (a) RuCOF-100' and (c) RuCOF-101'. The initial catalytic rates (obtained by linear fitting between 10 and 25 s of oxygen evolution curve) of (b) RuCOF-100' and (d) RuCOF-101' in five runs.

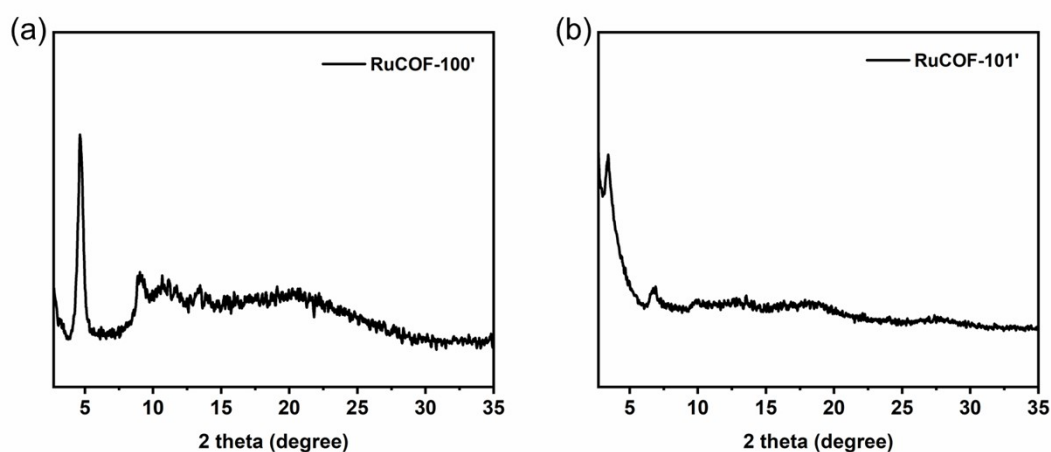


Fig. S44 PXRD patterns of RuCOF-100' and RuCOF-101' after five catalytic runs in chemical water oxidation.

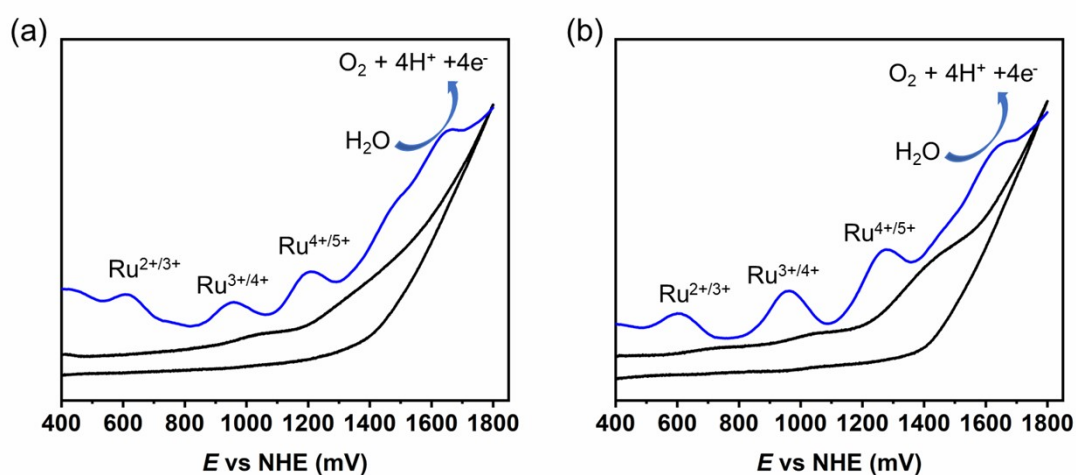


Fig. S45 Cyclic (black line) and differential pulse voltammograms (blue line) of (a) RuCOF-100' and (b) RuCOF-101'.

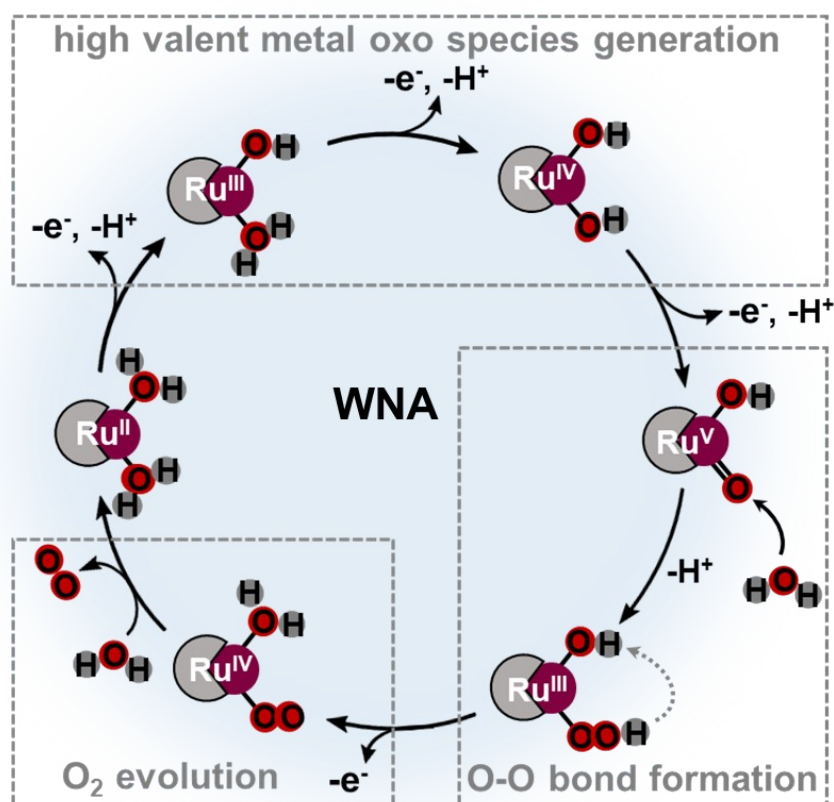


Fig. S46 Proposed mechanism for water oxidation with RuCOFs WOCs.

Due to the crystalline structures with integrating molecular ruthenium catalytic units, the as-synthesized RuCOFs are potential water oxidation catalysts. There are two general

pathways for O-O bond formation that are water nucleophilic attack (WNA) and interaction of two M-O units (I2M). Notably, there are two distinct features that allow differentiation between the two mechanisms by experiments. The WNA mechanism shows first-order kinetics with respect to catalyst concentration while in the I2M mechanism exhibits second-order kinetics. Besides, the WNA mechanism includes a proton coupled electron transfer in the rate determining step which is why strong H/D kinetic isotope effects can be expected on the rate of oxygen evolution if this pathway is occurring, thus leading to a ratio of $k_{\text{H}_2\text{O}} / k_{\text{D}_2\text{O}}$ of at least 2 in H_2O and D_2O . In contrast, for I2M mechanism, the ratio of $k_{\text{H}_2\text{O}} / k_{\text{D}_2\text{O}}$ is expected to be around 1.^[15, 16]

In this work, the first-order kinetics of chemical and photocatalytic water oxidation point to that they follow a similar WNA mechanism for the O-O bond formation. The kinetic isotope effect experiments also showed the ratio of $k_{\text{H}_2\text{O}} / k_{\text{D}_2\text{O}}$ are 2.43 for RuCOF-100' and 2.56 for RuCOF-101' (Figs. S39 and S40). Besides, in the electrochemical investigations, three consecutive oxidation peaks versus a normal hydrogen electrode (NHE) at +0.60, +0.95, and +1.20 V and +0.61, +0.97, and +1.26 V were detected for RuCOF-100' and RuCOF-101', respectively, which are assignable to the formal oxidation of $\text{Ru}^{2+/3+}$, $\text{Ru}^{3+/4+}$, and $\text{Ru}^{4+/5+}$ (Fig. S45). Therefore, based on our experimental results and related literatures, a possible WNA mechanistic pathway was described (Fig. S46). Catalysis initially starts with Ru(II) that is stepwise-oxidized to high valent Ru(V)=O intermediate. Then, the nucleophilic attack of a water molecule on the reactive Ru(V)=O species, forming the Ru(III)-OOH peroxide species that further suffers an proton-coupled electron transfer process to form Ru(IV)-OO. This subsequently releases dioxygen and coordinates substrate water molecules, consequently subjecting to the next catalytic cycle.

4.4 Computational models and methods

Density functional theory (DFT) calculation were performed to further investigate the catalytic mechanism. The hybrid B3LYP exchange-correlation functional was adopted, and the 6-31G(d) basis set for C, H, O, N atoms and LANL2DZ basis set for Ru atoms. The unrestricted method is applied to the open-shell system. All calculations were carried out using Gaussian 09 software package.^[17] The calculated model was constructed based on the single-crystal structure of model complex $\text{Ru}(\text{bpy-Ph})_2\text{Cl}_2$, where the Cl ligands were replaced to generate several of the proposed intermediates. Geometry optimizations were then performed for each of the proposed intermediates. Subsequently, the calculation of single-point energy for the optimized intermediates were carried out.

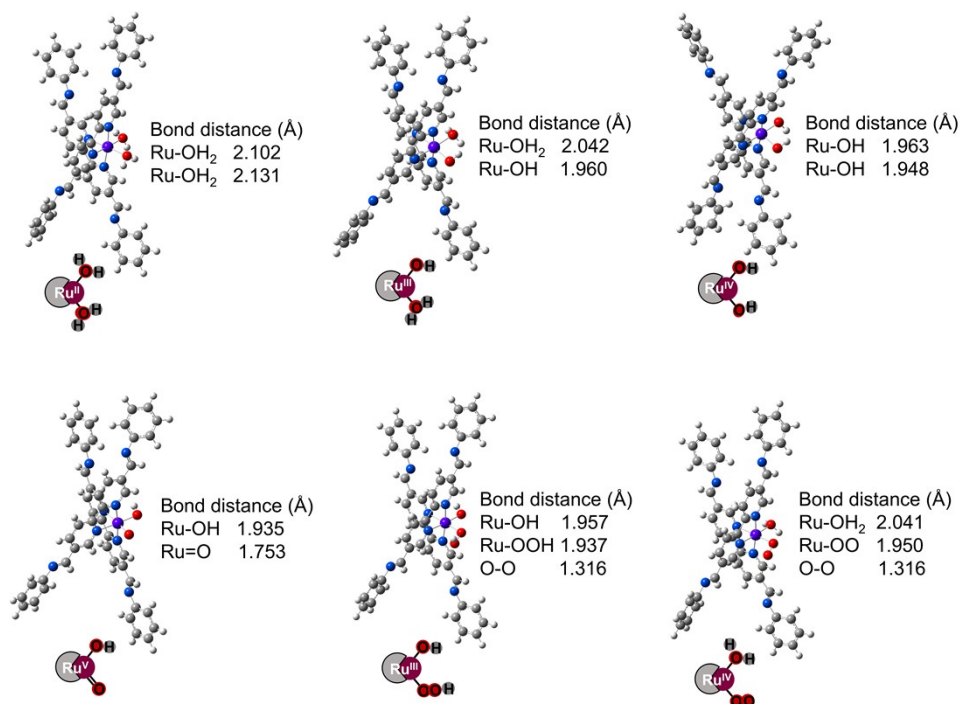
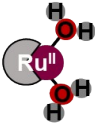
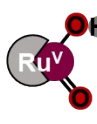
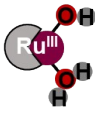
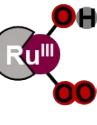
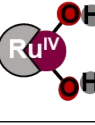
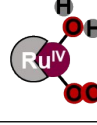


Fig. S47 Summary of the DFT optimized geometries for the proposed intermediates.

Table. S4 Summary of the free energies (Hartree) for the DFT optimized intermediates.

Species	Free energies (Hartree)	Species	Free energies (Hartree)
	-2534.5208565		-2532.6059517
	-2533.9015446		-2608.3077153
	-2533.2694449		-2608.2650602
H ₂ O	-76.3856887	H ₂	-1.1562657

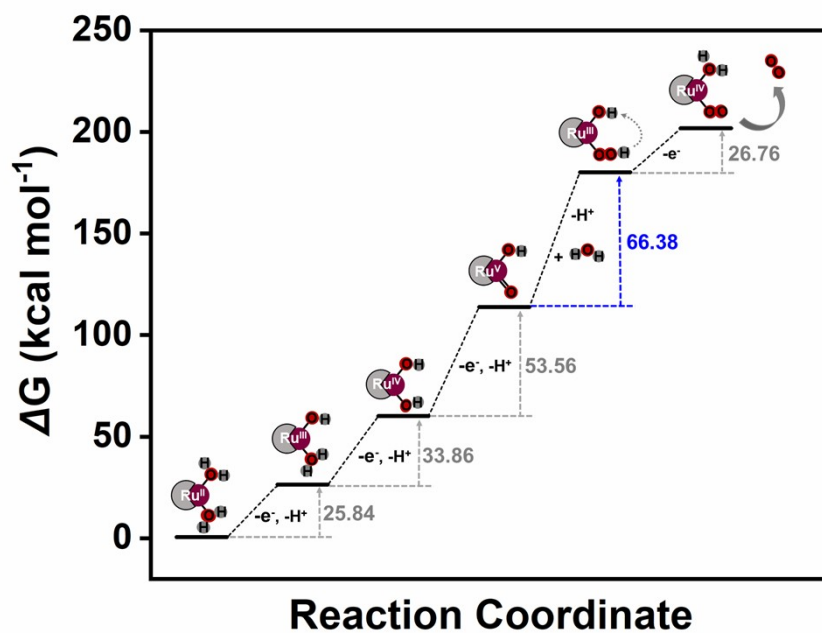


Fig. S48 Free energy diagram for O₂ evolution from water oxidation over MCOFs.

The DFT calculation of free energy were performed to explore the water oxidation pathway on the as-synthesized MCOFs. As shown in Fig. S48, two water molecular were absorbed on the Ru site. It has been widely postulated that the Ru^V=O intermediate is an active species required for water activation in molecular Ru catalysts. Indeed, The DFT calculation predicted a Ru-O distance of 1.753 Å for the proposed intermediate, which is consistent with the bond distance of Ru^V=O reported in literature (about 1.7 Å).^[18] Besides, the calculated result suggested that the O-O bond formation is the rate-determining step of the reaction, as judged by the largest energy barrier of 66.38 kcal mol⁻¹.

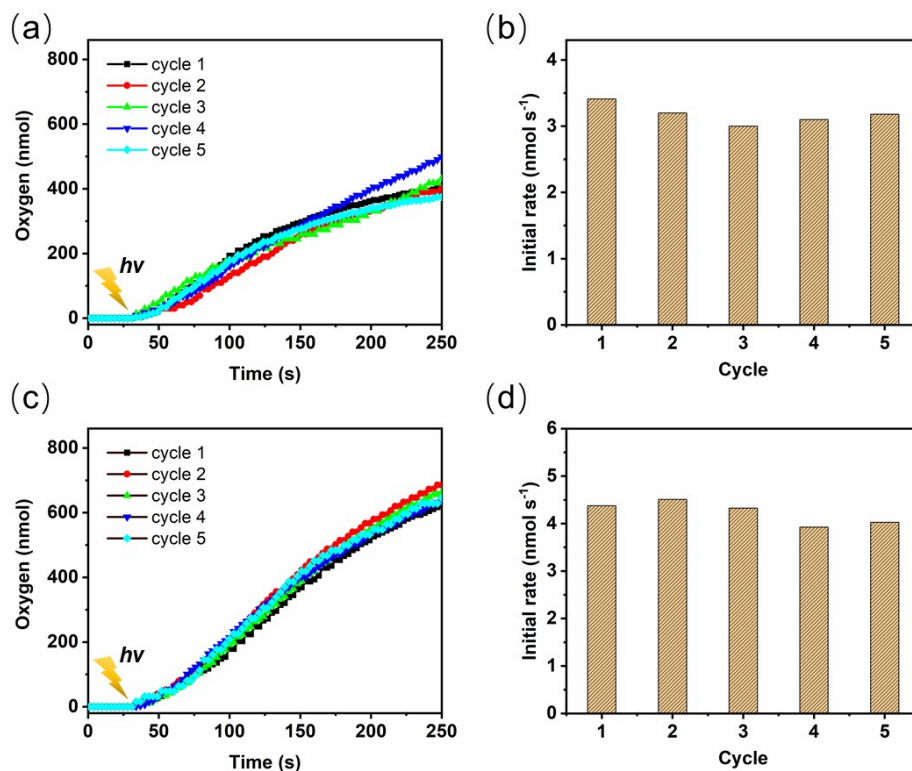


Fig. S49 The recyclability of photocatalytic water oxidation (WOC concentration 0.45 g L⁻¹): The time-dependent oxygen evolution of (a) RuCOF-100' and (c) RuCOF-101'. Irradiation started at t = 30s. The initial catalytic rates (obtained by linear fitting between 90 and 110 s of oxygen evolution curve) of (b) RuCOF-100' and (d) RuCOF-101' in five runs.

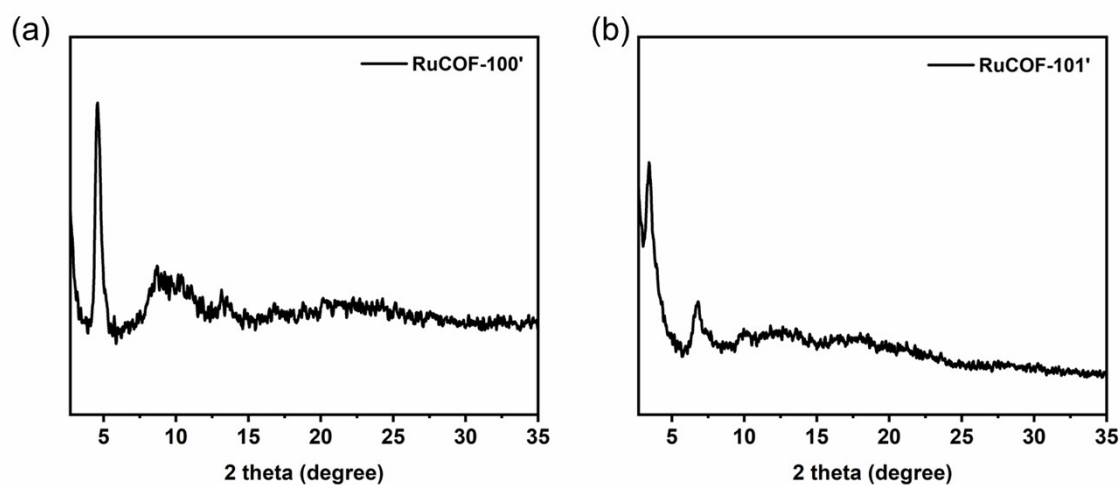


Fig. S50 PXRD patterns of RuCOF-100' and RuCOF-101' after five catalytic runs in photocatalytic water oxidation.

4.5 Comparison of photocatalytic O₂ evolution activity

Table S5. The comparison of photocatalytic O₂ evolution activity of typical COFs-based heterogeneous photocatalysts.

Photocatalyst	Irradiation	O ₂ evolution rate	References
RuCOF-100'	$\lambda > 420$ nm	315 nmol g ⁻¹ s ⁻¹	This work
RuCOF-101'	$\lambda > 420$ nm	425 nmol g ⁻¹ s ⁻¹	
BtB-COF	$\lambda > 420$ nm	185 nmol g ⁻¹ s ⁻¹	19
Bpy-CTF-Co-3	$\lambda > 420$ nm	89 nmol g ⁻¹ s ⁻¹	20
CTF-1-100W	$\lambda > 420$ nm	39 nmol g ⁻¹ s ⁻¹	21
CTF-T1	$\lambda > 420$ nm	2.5 nmol g ⁻¹ s ⁻¹	22
g-C ₄₀ N ₃ -COF	$\lambda > 420$ nm	13.8 nmol g ⁻¹ s ⁻¹	23
g-C ₅₄ N ₆ -COF	$\lambda > 420$ nm	14.2 nmol g ⁻¹ s ⁻¹	24
CTF-0-I	$\lambda > 420$ nm	16.4 nmol g ⁻¹ s ⁻¹	25
sp ² -c-COF	$\lambda > 420$ nm	6 nmol g ⁻¹ s ⁻¹	26
r-CTF NSs	$\lambda > 420$ nm	68 nmol g ⁻¹ s ⁻¹	27
I-TST	$\lambda > 420$ nm	4.7 nmol g ⁻¹ s ⁻¹	28
BpCo-COF-1	$\lambda > 420$ nm	42 nmol g ⁻¹ s ⁻¹	29
BpCo-COF-1	AM 1.5G	76 nmol g ⁻¹ s ⁻¹	
Pt@TpBpy-NS	$\lambda > 420$ nm	17.8 nmol g ⁻¹ s ⁻¹	30
Pt@TpBpy-2-NS	$\lambda > 420$ nm	5.3 nmol g ⁻¹ s ⁻¹	

4.6 Electrochemical O₂ evolution activity

For the experiment of electrochemical O₂ evolution, the catalyst (5 mg) with carbon black (1 mg) were ultrasonic dispersed in a Nafion ethanol solution (0.25 wt.%, 500 μ L) for 2 h to yield a homogeneous ink. The catalyst ink (40 μ L) was pipetted onto a NF (1 \times 1 cm²) with a loading amount of 0.4 mg cm⁻². Hg/HgO electrode and Pt plate were served as counter electrode and reference electrode, respectively. Linear sweep voltammogram (LSV) curves were got at low scan rate (10 mV s⁻¹) in aqueous solution of KOH (0.1 M). Tafel slopes could be got according the prominent equation ($\eta = a + b \log j$) through the LSV curves.

The linear sweep voltammogram measurement was conducted to assess the O₂ evolution activity of the as-prepared MCOFs-based catalysts, showing the overpotential of 400 and 370 mV for RuCOF-100' and RuCOF-101', respectively, to drive the water oxidation reaction at 10 mA cm⁻² (Fig. S51). The Tafel slopes of RuCOF-100' and RuCOF-101' were estimated to be 175 and 167 mV dec⁻¹, respectively.

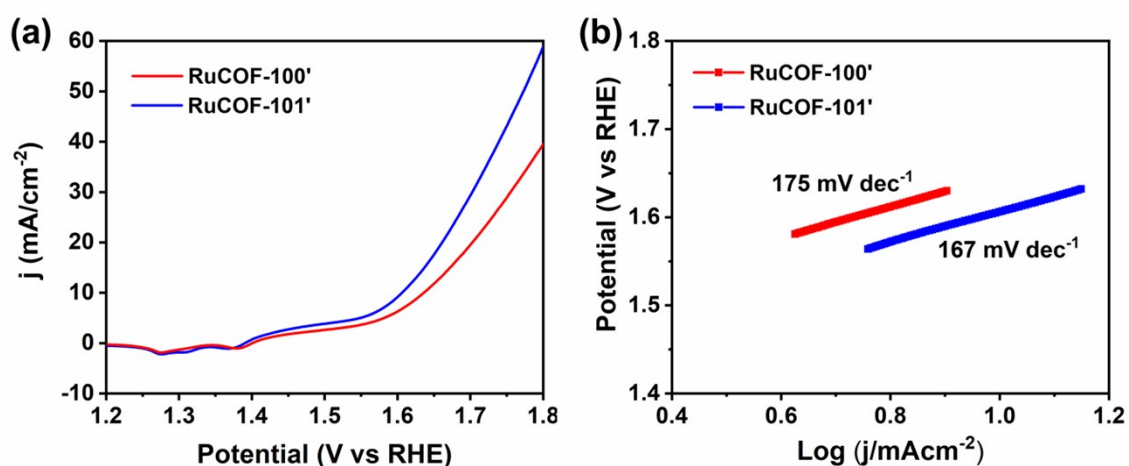


Fig. S51 (a) LSV curves and (b) Tafel plots for MCOFs.

Section 5. Oxidation of organic substrates

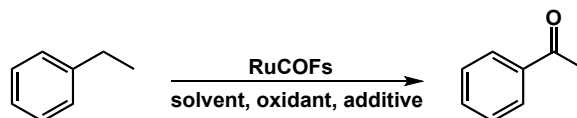
Selective oxidation of organic compounds is one of the most fundamental reactions in organic synthesis and industrial chemistry. Especially, the selective oxidation of inert C-H bond has attracted great attention but full of challenges.^[31, 32] Due to the rich oxidative properties of the Ru=O species, a large number of examples related to ruthenium catalysts have emerged recently. Herein, to demonstrate the general applicability of our strategy for integrating molecular ruthenium catalyst into MCOFs, our reported RuCOFs were further used to catalyze selective oxidation of sp³ C-H bonds to carbonyls. Initially, we used ethylbenzene as the model substrate to evaluate the reaction parameters (Table S6). The reaction was first performed by using RuCOFs as catalysts with different oxidant. CAN was founded to be the best oxidant for this reaction. Further experiments showed that the addition of a chloride scavenger, AgNO₃, can led to demonstrative improvement in catalytic yields. It is speculated that the coordinated Cl were removed by Ag⁺, accelerating the formation of active high valent Ru(V)=O species. With the optimal reaction conditions, we next explored the scope of substrates with C-H bonds. Gratifyingly, the conversion of various substrates catalyzed by the our RuCOFs exhibited considerable yields (Table S7). Control experiments showed that the reaction can hardly occur without RuCOFs catalysts, verifying the RuCOFs played a catalytic role in the reaction. In addition, the solid catalyst could be easily recovered, and their catalytic activity showed only slight change after recycling five runs.

5.1 Typical procedure for selective oxidation of sp³ C-H bonds

Typical procedure for selective oxidation of sp³ C-H bonds: Organic substrate (0.25 mmol), RuCOF (10 mg), CAN (0.75 mmol) and MeCN/H₂O (3 mL/1 mL) was added into a 10 mL glass vessel with a stir bar. After stirring the mixture at room temperature overnight, the catalyst was isolated by centrifugation, and the supernatant was extracted with EtOAc. The organic phase was washed with brine and dried over anhydrous Mg₂SO₄, concentrated in vacuum, and the resulting residue was purified by flash column chromatography (PE/EtOAc) to afford the desired product. For cyclic experiments, the separated catalyst was washed with DMF and THF five times and then dried in a vacuum for overnight at 60 °C, and the dried catalyst was used for the next experiment.

5.2 Catalytic performance for selective oxidation of sp³ C-H bonds

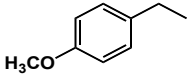
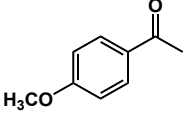
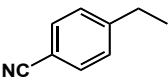
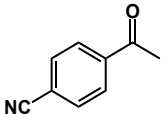
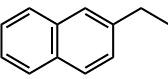
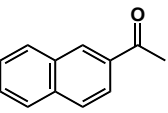
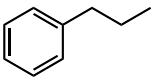
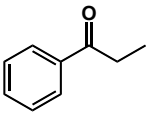
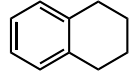
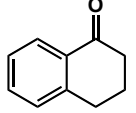
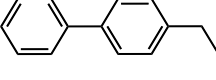
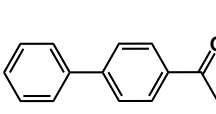
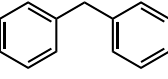
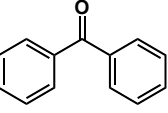
Table S6. Optimization of the reaction conditions for selective oxidation of sp³ C-H bonds [a]



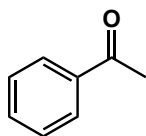
Entry	Catalyst	Oxidant	Additive [b]	Yield (%) [c]
1	RuCOF-100 (5 mg)	/	/	Trace
2	RuCOF-100 (5 mg)	NaIO ₄	/	38
3	RuCOF-100 (5 mg)	Oxone	/	19
4	RuCOF-100 (5 mg)	CAN	/	47
5	RuCOF-100 (5 mg)	KBrO ₃	/	32
6	RuCOF-100 (5 mg)	CAN	AgNO ₃	53
7	/	CAN	AgNO ₃	< 5
8	RuCOF-100 (10 mg)	CAN	AgNO ₃	65
9	RuCOF-101 (10 mg)	CAN	AgNO ₃	76
10	RuCOF-101 (10 mg) (2 nd -use)	CAN	AgNO ₃	79
11	RuCOF-101 (10 mg) (3 rd -use)	CAN	AgNO ₃	74
12	RuCOF-101 (10 mg) (4 th -use)	CAN	AgNO ₃	72
13	RuCOF-101 (10 mg) (5 th -use)	CAN	AgNO ₃	75

[a] Reaction conditions: substrates (0.25 mmol), catalyst, oxidant (0.75 mmol), MeCN/H₂O (3 mL/1 mL). The reaction mixture was stirred at room temperature overnight. [b] 10 mg of additive was used. [c] Yields of the isolated products.

Table S7. The selective oxidation of sp^3 C-H bonds by using RuCOF-101 catalyst ^[a]

Entry	substrate	product	Yield (%) ^[b]
1			75
2			69
3			61
4			73
5			82
6			63
7			78

[a] Reaction conditions: substrates (0.25 mmol), catalyst (10 mg), CAN (0.75 mmol), 10 mg of $AgNO_3$ additive, MeCN/ H_2O (3 mL/1 mL). The reaction mixture was stirred at room temperature overnight. [b] Yields of the isolated products.



Acetophenone: Colorless oil. ^1H NMR (400 MHz, CDCl_3 , δ : ppm) 7.97 (d, 2H, ArH), 7.58-7.54 (m, 1H, ArH), 7.48-7.44 (m, 2H, ArH), 2.60 (s, 3H, CH_3). ^{13}C NMR (101 MHz, CDCl_3 , δ : ppm) 198.11, 137.17, 133.09, 128.57, 128.30, 26.58.

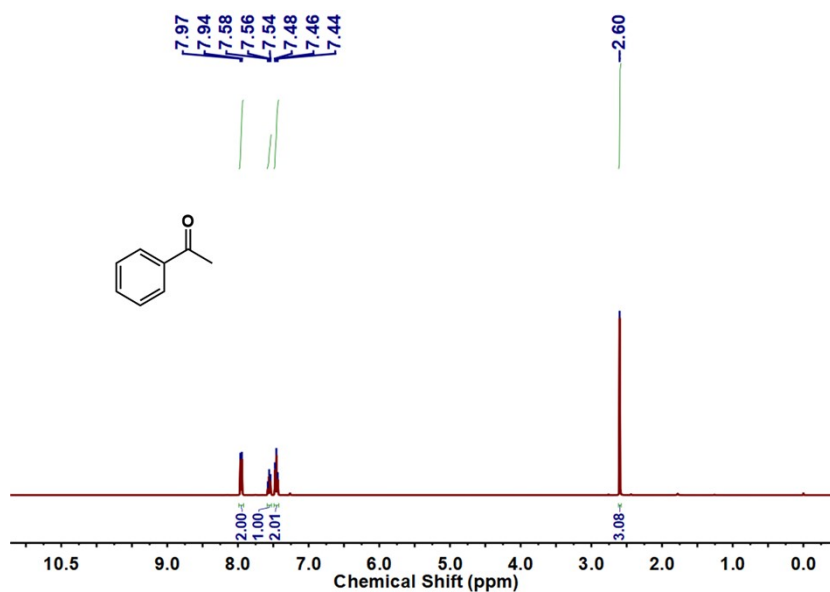


Fig. S52 ^1H NMR spectrum of acetophenone.

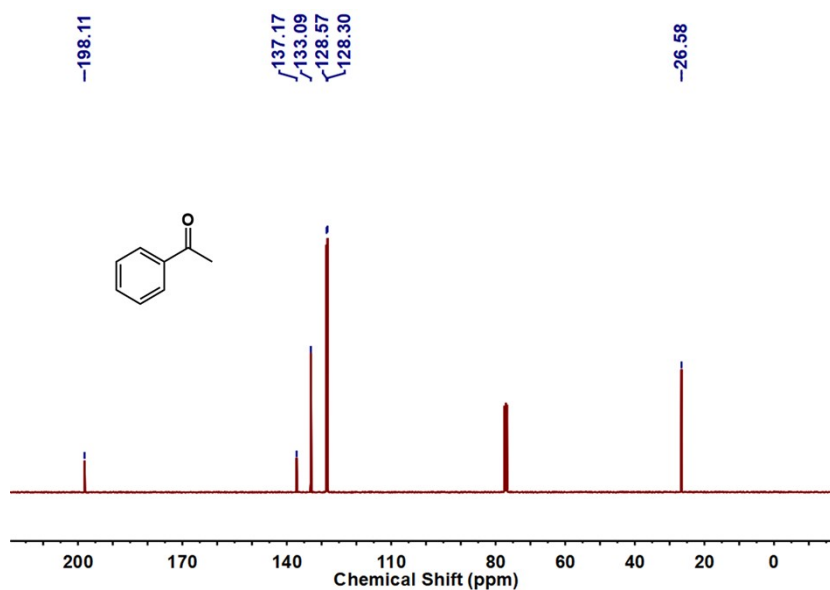
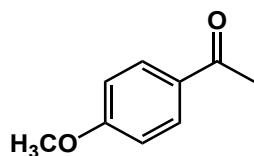


Fig. S53 ^{13}C NMR spectrum of acetophenone.



4-methoxyacetophenone: Colorless oil. ^1H NMR (400 MHz, CDCl_3 , δ : ppm) 7.94 (d, 2H, ArH), 6.94 (d, 2H, ArH), 3.86 (s, 3H, OCH_3), 2.55 (s, 3H, CH_3). ^{13}C NMR (101 MHz, CDCl_3 , δ : ppm) 196.74, 163.50, 130.58, 113.69, 55.72, 26.31.

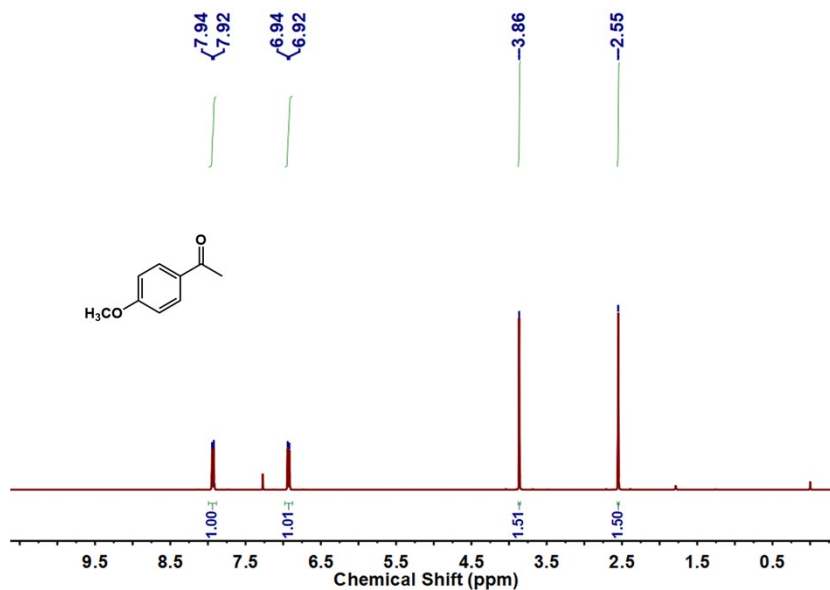


Fig. S54 ^1H NMR spectrum of 4-methoxyacetophenone.

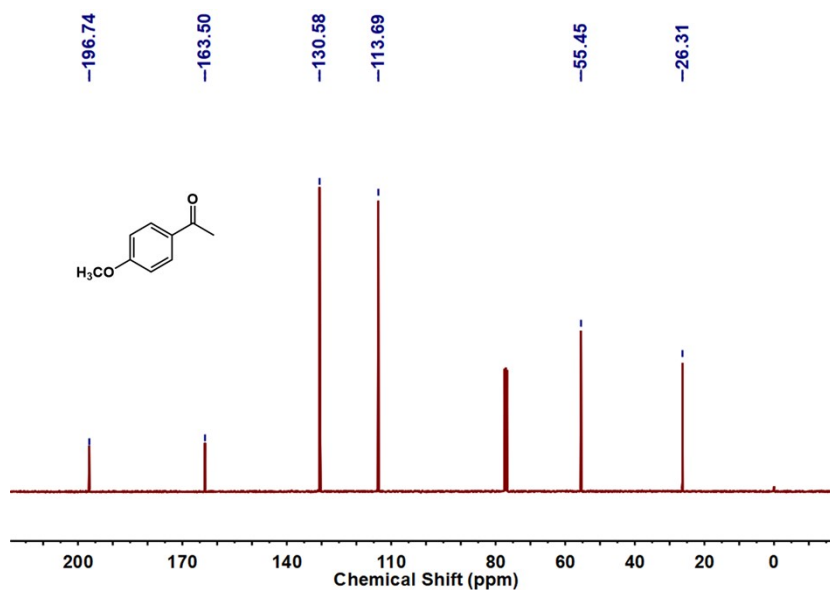
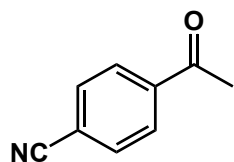


Fig. S55 ^{13}C NMR spectrum of 4-methoxyacetophenone.



4-acetylbenzonitrile: Colorless oil. ^1H NMR (400 MHz, CDCl_3 , δ : ppm) 8.06 (d, 2H, ArH), 7.79 (d, 2H, ArH), 2.65 (s, 3H, CH_3). ^{13}C NMR (101 MHz, CDCl_3 , δ : ppm) 196.48, 139.96, 132.52, 128.70, 117.91, 116.46, 26.74.

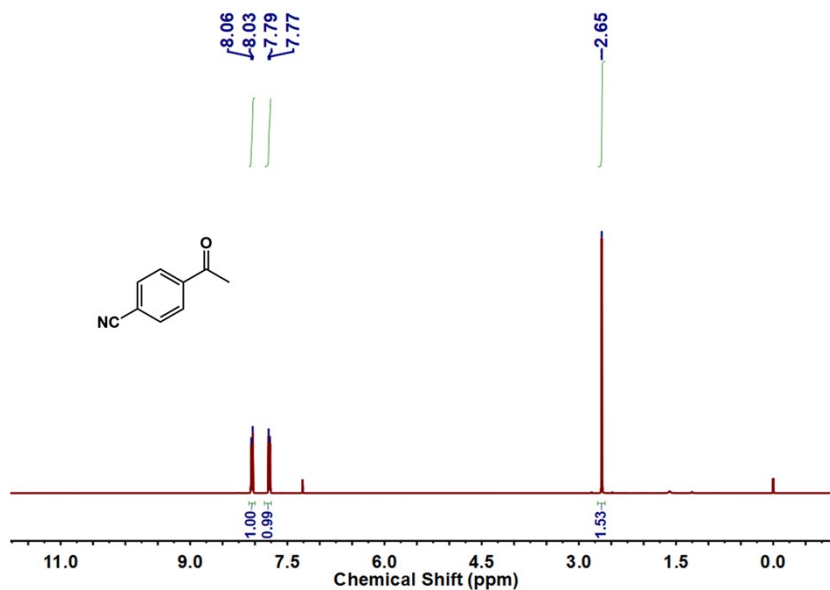


Fig. S56 ^1H NMR spectrum of 4-acetylbenzonitrile.

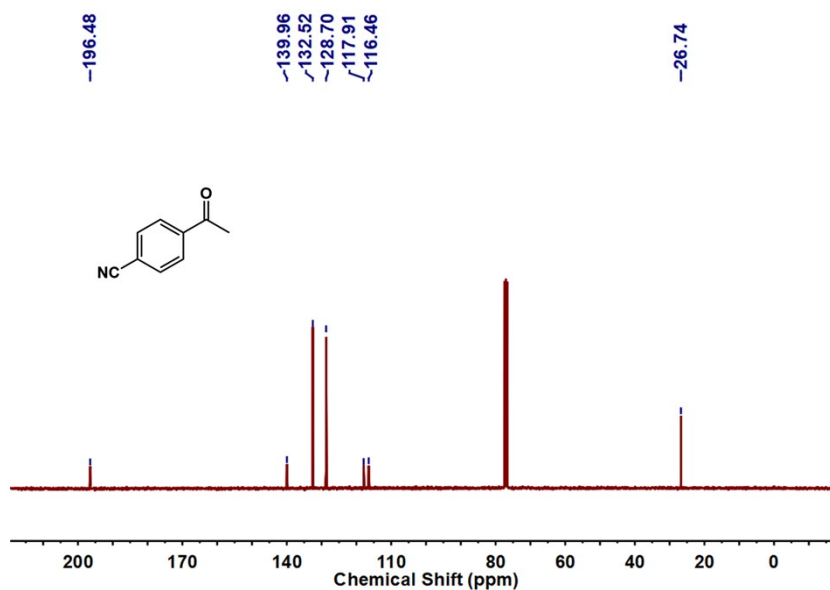
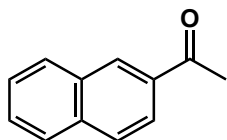


Fig. S57 ^{13}C NMR spectrum of 4-acetylbenzonitrile.



2-acetonaphthone: White solid. ^1H NMR (400 MHz, CDCl_3 , δ : ppm) 8.46 (s, 1H, ArH), 8.04-8.02 (m, 1H, ArH), 7.97 (d, 1H, ArH), 7.90-7.86 (m, 2H, ArH), 7.61-7.53 (m, 2H, ArH), 2.72 (s, 3H, CH_3). ^{13}C NMR (101 MHz, CDCl_3 , δ : ppm) 198.07, 135.62, 134.55, 132.55, 130.19, 129.56, 128.47, 128.43, 127.80, 126.78, 123.92, 26.68.

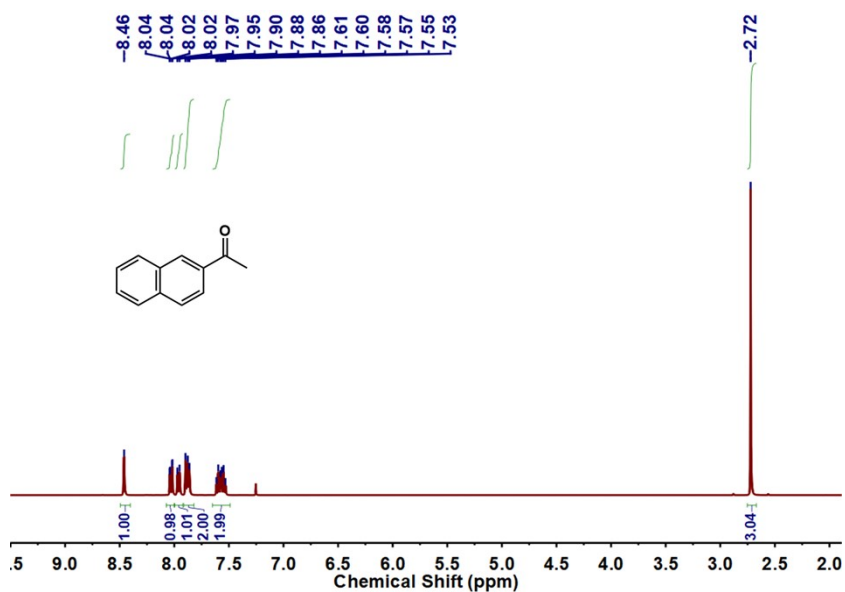


Fig. S58 ^1H NMR spectrum of 2-acetonaphthone.

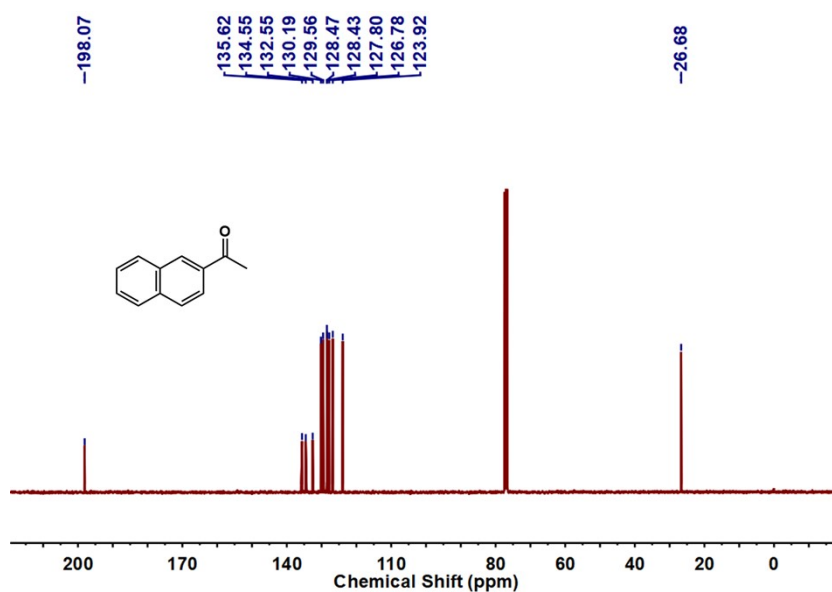
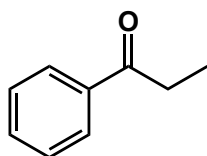


Fig. S59 ^{13}C NMR spectrum of 2-acetonaphthone.



Propiophenone: Colorless oil. ^1H NMR (400 MHz, CDCl_3 , δ : ppm) 7.95 (s, 2H, ArH), 7.53 (s, 1H, ArH), 7.44 (s, 2H, ArH), 2.08 (m, 2H, CH_2), 3.09 (m, 3H, CH_3). ^{13}C NMR (101 MHz, CDCl_3 , δ : ppm) 200.78, 136.95, 132.85, 128.54, 127.96, 31.76, 8.23.

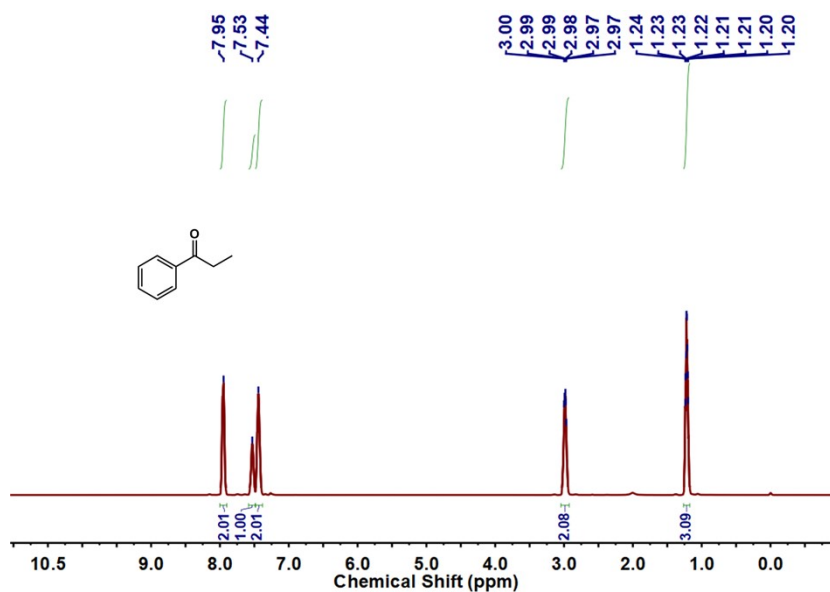


Fig. S60 ^1H NMR spectrum of propiophenone.

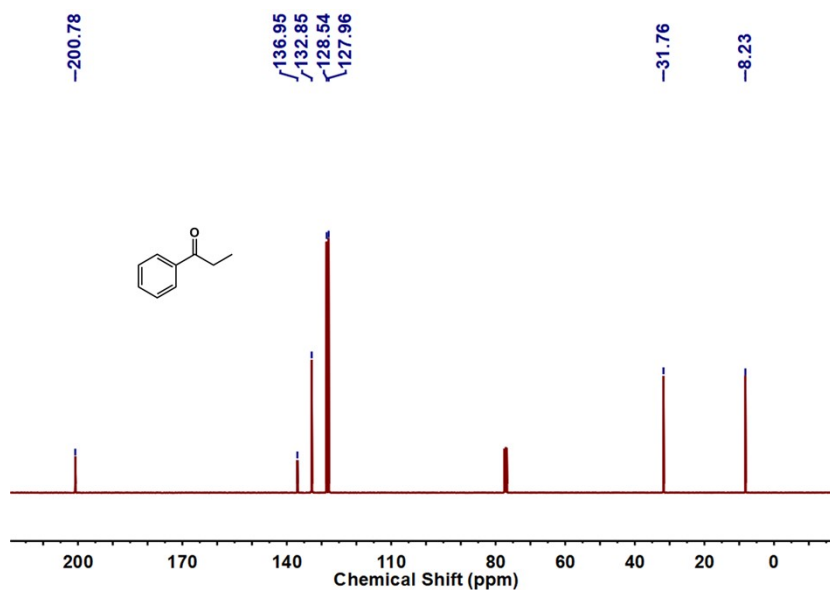
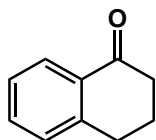


Fig. S61 ^{13}C NMR spectrum of propiophenone.



1-tetralone: Colorless oil. ^1H NMR (400 MHz, CDCl_3 , δ : ppm) 8.03 (d, 1H, ArH), 7.46-7.43 (m, 1H, ArH), 7.30-7.22 (m, 2H, ArH), 2.96-2.93 (m, 2H, CH_2), 2.65-2.62 (m, 2H, CH_2), 2.15-2.09 (m, 2H, CH_2). ^{13}C NMR (101 MHz, CDCl_3 , δ : ppm) 198.28, 144.48, 133.37, 132.63, 128.78, 127.13, 126.60, 39.16, 29.70, 23.29.

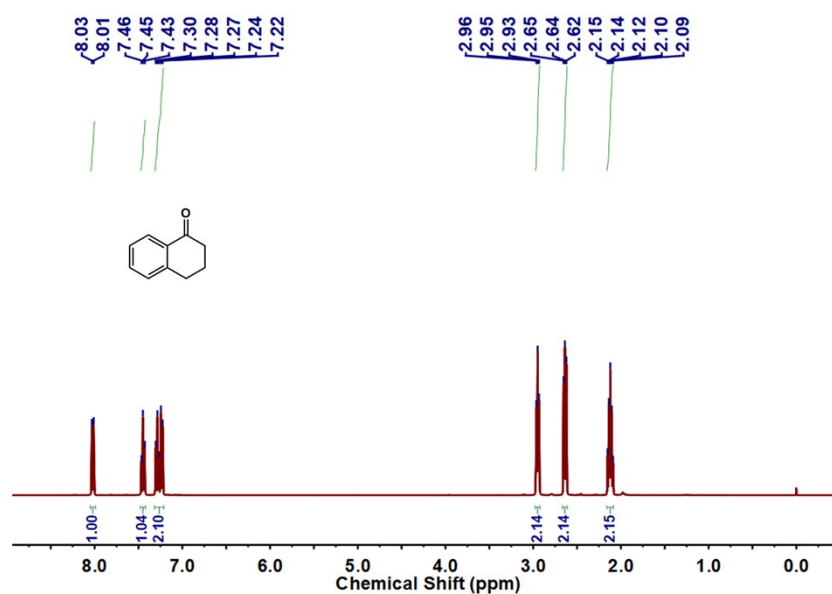


Fig. S62 ^1H NMR spectrum of 1-tetralone.

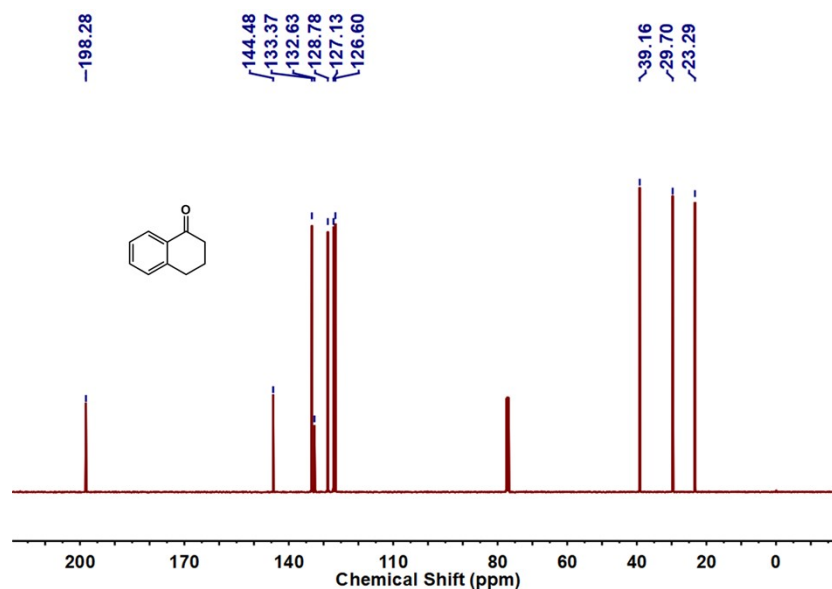
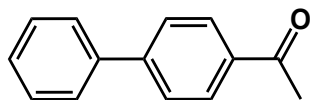


Fig. S63 ^{13}C NMR spectrum of 1-tetralone.



4-acetylbiphenyl: White solid. ^1H NMR (400 MHz, CDCl_3 , δ : ppm) 8.04-8.02 (d, 2H, ArH), 7.69-7.67 (m, 2H, ArH), 7.63-7.62 (m, 2H, ArH), 7.49-7.40 (m, 3H, ArH), 2.63 (s, 3H, CH_3). ^{13}C NMR (101 MHz, CDCl_3 , δ : ppm) 197.73, 145.80, 139.91, 135.91, 128.96, 128.92, 128.24, 127.28, 127.24, 26.65.

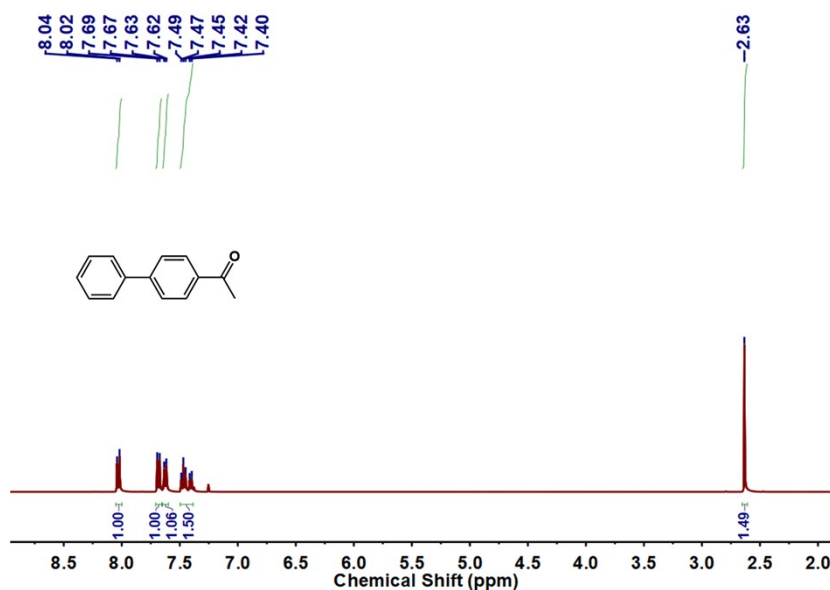


Fig. S64 ^1H NMR spectrum of 4-acetylbiphenyl.

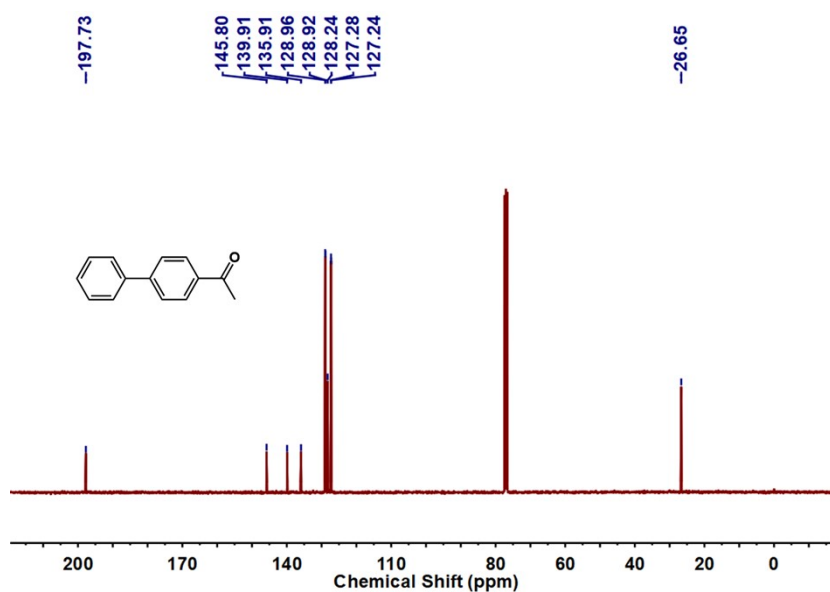
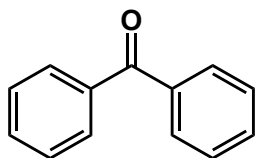


Fig. S65 ^{13}C NMR spectrum of 4-acetylbiphenyl.



Benzophenone: White solid. ^1H NMR (400 MHz, CDCl_3 , δ : ppm) 7.81-7.79 (m, 4H, ArH), 7.59-7.58 (m, 2H, ArH), 7.50-7.47 (m, 4H, ArH). ^{13}C NMR (101 MHz, CDCl_3 , δ : ppm) 196.74, 137.65, 132.41, 130.06, 128.28.

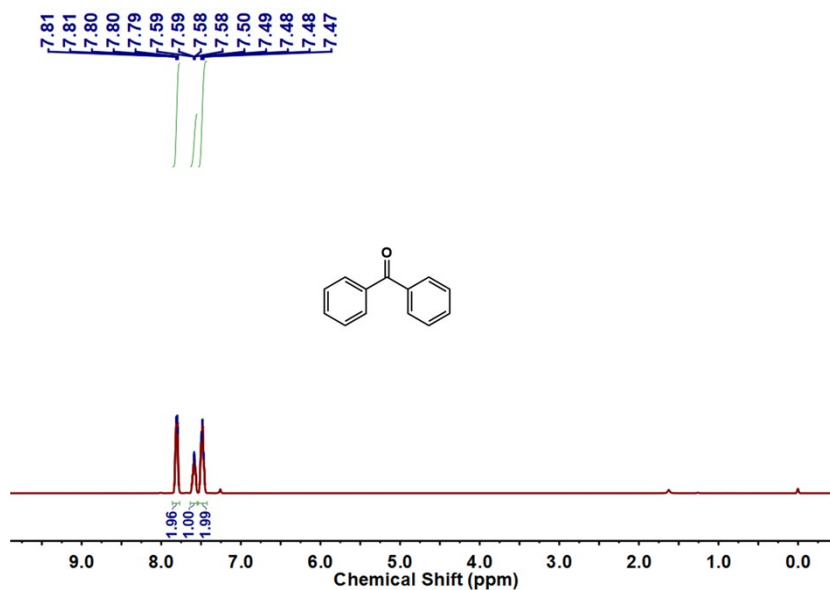


Fig. S66 ^1H NMR spectrum of benzophenone.

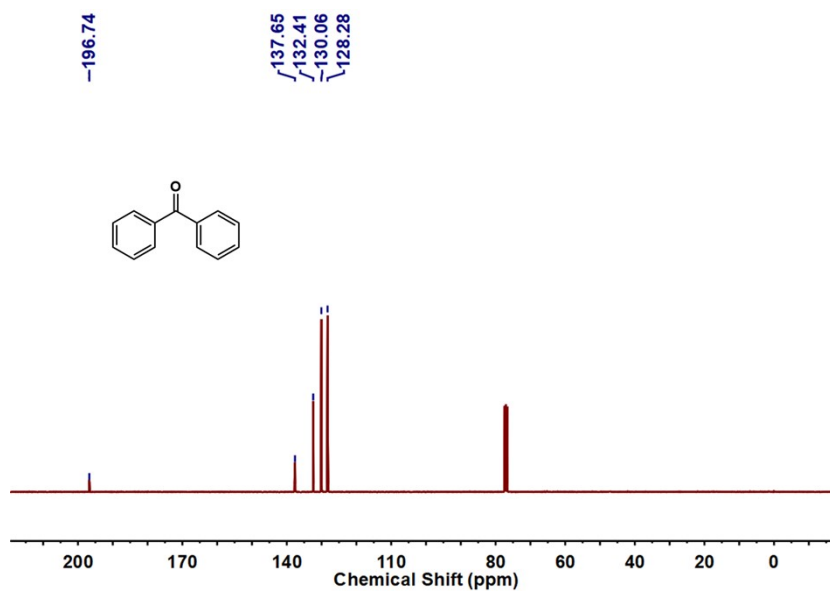


Fig. S67 ^{13}C NMR spectrum of benzophenone.

Section 6. Unit cell parameters and fractional atomic coordinates

Table S8. Unit cell parameters and fractional atomic coordinates for RuCOF-100.

Space group: <i>Pnc2</i>			
Cell parameters: $a = 22.69 \text{ \AA}$, $b = 32.91 \text{ \AA}$, $c = 23.44 \text{ \AA}$, $\alpha = \beta = \gamma = 90^\circ$			
Atom	x(\AA)	y(\AA)	z(\AA)
C1	0.72541	0.27754	0.26704
C2	0.7854	0.26803	0.27963
N3	0.9086	0.0204	0.485
C4	0.88706	0.05366	0.45769
C5	0.8287	0.06885	0.47099
C6	0.8072	0.10633	0.44353
N7	0.84034	0.12259	0.40351
N8	0.96824	0.96045	0.54147
C9	0.90917	0.96786	0.55795
C10	0.8843	0.94566	0.60363
C11	0.92129	0.91626	0.63079
C12	0.98187	0.90945	0.61169
C13	0.0045	0.93226	0.56653
C14	0.79359	0.04924	0.51305
C15	0.81739	0.0151	0.54151
C16	0.8764	1.00111	0.52705
N17	0.01714	0.86325	0.68648
C18	0.02505	0.88076	0.63755
C19	0.6352	0.42333	0.09716
N20	0.66976	0.42276	0.14227
N21	0.44695	0.66015	0.84735
C22	0.48849	0.66642	0.88614
N23	0.4323	0.50513	-0.0079
N24	0.52716	0.56129	0.93353
C25	0.63762	0.53326	0.04928
C26	0.40578	0.46877	0.00519
C27	0.41934	0.53992	0.02078
C28	0.4068	0.39303	-0.01631
C29	0.42778	0.43254	0.9731
C30	0.37659	0.53915	0.06527
C31	0.56661	0.63935	0.95372
C32	0.65214	0.49775	0.07934
C33	0.50038	0.59214	0.90421
C34	0.5199	0.63214	0.91372
C135	0.57668	0.01114	0.35573
C136	0.97	0.54784	0.90555
C37	0.82625	0.15964	0.37463
C38	0.93589	0.33682	0.20863
C39	0.68146	0.3864	0.17415
C40	0.58966	0.19155	0.32208
C41	0.71922	0.38837	0.22242
C42	0.73258	0.35321	0.25353
C43	0.70844	0.3155	0.2366
C44	0.66948	0.31369	0.18898
C45	0.65609	0.34883	0.15792
C46	0.78129	0.18666	0.39486
C47	0.76909	0.22257	0.36508

C48	0.80117	0.23171	0.31456
C49	0.8471	0.20502	0.29554
C50	0.85967	0.16936	0.32553
C51	0.63327	0.18068	0.28093
C52	0.67546	0.20927	0.26068
C53	0.6747	0.24918	0.28162
C54	0.62957	0.26062	0.32127
C55	0.58727	0.23193	0.34153
C56	0.8871	0.3234	0.17387
C57	0.83892	0.30065	0.19673
C58	0.83784	0.29132	0.25502
C59	0.88747	0.3035	0.28951
C60	0.93615	0.3262	0.26645
H61	0.91494	0.06975	0.42412
H62	0.76363	0.12123	0.45578
H63	0.83682	0.95159	0.6172
H64	0.90371	0.89762	0.66807
H65	0.05174	0.92716	0.55158
H66	0.74754	0.06114	0.52305
H67	0.79039	-0.00125	0.5755
H68	0.06681	0.87448	0.61197
H69	0.61342	0.3941	0.08179
H70	0.50077	0.69875	0.89898
H71	0.65992	0.56342	0.0596
H72	0.44265	0.56947	0.00917
H73	0.36954	0.38803	0.01556
H74	0.58219	0.67187	0.96113
H75	0.6867	0.49882	0.11461
H76	0.46324	0.5851	0.87298
H77	0.73869	0.41886	0.23577
H78	0.76279	0.35511	0.2923
H79	0.64895	0.28347	0.17593
H80	0.62495	0.34708	0.11984
H81	0.75547	0.17893	0.43515
H82	0.73368	0.24424	0.38137
H83	0.87363	0.21283	0.25573
H84	0.89654	0.14844	0.31038
H85	0.63375	0.14813	0.26426
H86	0.70958	0.19966	0.22762
H87	0.62689	0.29327	0.33735
H88	0.55195	0.24184	0.3732
H89	0.8879	0.33157	0.12662
H90	0.80166	0.29021	0.16757
H91	0.88898	0.29515	0.33667
H92	0.97444	0.33537	0.2952
Ru93	0	0	0.47811
Ru94	0.5	0.5	0.92832

Table S9. Unit cell parameters and fractional atomic coordinates for RuCOF-101.

Space group: <i>Pnc2</i>			
Cell parameters: $a = 30.96 \text{ \AA}$, $b = 44.47 \text{ \AA}$, $c = 31.31 \text{ \AA}$, $\alpha = \beta = \gamma = 90^\circ$			
Atom	x(Å)	y(Å)	z(Å)
C1	0.73106	0.26219	0.26498
C2	0.77259	0.25617	0.26801
C3	0.85353	0.10111	0.40381
C4	0.81276	0.11221	0.40866
C5	0.80005	0.13777	0.38704
C6	0.82771	0.1526	0.36031
C7	0.86833	0.14141	0.35571
C8	0.88099	0.11598	0.37732
C9	0.94728	0.36958	0.14023
C10	0.9052	0.3674	0.12808
C11	0.87799	0.34816	0.14868
C12	0.89209	0.33024	0.18144
C13	0.93428	0.33199	0.19299
C14	0.96151	0.35142	0.17249
C15	0.64396	0.41766	0.13346
C16	0.68506	0.41613	0.14773
C17	0.69896	0.39116	0.16979
C18	0.67167	0.36734	0.17855
C19	0.63011	0.36927	0.1651
C20	0.61633	0.39416	0.14285
C21	0.56677	0.13907	0.3877
C22	0.60682	0.13099	0.37483
C23	0.63171	0.15116	0.35307
C24	0.61676	0.17987	0.34322
C25	0.57621	0.18783	0.35552
C26	0.55135	0.16764	0.3775
N27	0.93511	0.0069	0.48498
C28	0.9143	0.02842	0.46382
C29	0.87157	0.03279	0.47063
C30	0.84896	0.05733	0.44978
N31	0.86913	0.07549	0.42567
N32	0.98527	0.96839	0.52705
C33	0.94379	0.96724	0.53594
C34	0.92975	0.94658	0.56554
C35	0.95867	0.92788	0.58523
C36	1.00129	0.92996	0.57563
C37	0.0139	0.95075	0.54592
C38	0.8511	0.01402	0.49878
C39	0.87326	-0.0081	0.52016
C40	0.91623	0.98871	0.51315
N41	0.02351	0.88937	0.62029
C42	0.03329	0.9112	0.59562
C43	0.60021	0.44444	0.08478
N44	0.6311	0.44366	0.11066
N45	0.45711	0.61739	0.91033
C46	0.4902	0.62245	0.93234
N47	0.45372	0.50255	0.01372
N48	0.51648	0.54569	0.9713
C49	0.59547	0.52605	0.05225

C50	0.43608	0.47549	0.02232
C51	0.44248	0.52822	0.03322
C52	0.43838	0.41952	0.0048
C53	0.45246	0.449	0.99907
C54	0.4113	0.5276	0.06338
C55	0.54313	0.6037	0.98241
C56	0.6078	0.49992	0.07264
C57	0.49792	0.56787	0.9493
C58	0.51072	0.59768	0.95463
C159	0.55238	0.00587	0.41524
C160	0.987	0.53692	0.92863
C61	0.81439	0.17961	0.33715
C62	0.86264	0.3101	0.20347
C63	0.68647	0.34049	0.20135
C64	0.64378	0.20147	0.32089
C65	0.71471	0.34332	0.2343
C66	0.72895	0.31798	0.25528
C67	0.7154	0.28933	0.24361
C68	0.6867	0.28645	0.21128
C69	0.67254	0.31174	0.1902
C70	0.79013	0.20184	0.35627
C71	0.77742	0.22713	0.33424
C72	0.78823	0.23044	0.29254
C73	0.8132	0.20864	0.27367
C74	0.82607	0.18342	0.2957
C75	0.67039	0.19162	0.28922
C76	0.69789	0.2115	0.27018
C77	0.69946	0.24158	0.28255
C78	0.67176	0.25182	0.31283
C79	0.64429	0.23192	0.33201
C80	0.83107	0.29495	0.18175
C81	0.80208	0.27723	0.2026
C82	0.80403	0.27429	0.24559
C83	0.8362	0.28853	0.26729
C84	0.8651	0.30643	0.24648
H85	0.79067	0.10159	0.42906
H86	0.76842	0.14574	0.39088
H87	0.89055	0.15257	0.33584
H88	0.91256	0.10785	0.37355
H89	0.89287	0.38014	0.10258
H90	0.84565	0.34762	0.13919
H91	0.94635	0.31813	0.21762
H92	0.99385	0.35246	0.18191
H93	0.70658	0.43418	0.14113
H94	0.73125	0.39028	0.17937
H95	0.60801	0.35171	0.17226
H96	0.58393	0.39511	0.13378
H97	0.61902	0.10903	0.38228
H98	0.66299	0.14444	0.34463
H99	0.56352	0.20957	0.34773
H100	0.52013	0.1744	0.38579
H101	0.93104	0.04259	0.44264
H102	0.816	0.06007	0.4555
H103	0.8972	0.94466	0.57356

H104	0.94778	0.91203	0.60807
H105	0.04641	0.95269	0.53784
H106	0.81812	0.01682	0.50475
H107	0.85689	-0.02188	0.5422
H108	0.06551	0.91643	0.58914
H109	0.58293	0.42429	0.07755
H110	0.50209	0.64494	0.93626
H111	0.61052	0.5469	0.06018
H112	0.45764	0.54907	0.02546
H113	0.41385	0.41412	0.02633
H114	0.55376	0.62645	0.98719
H115	0.632	0.50129	0.09581
H116	0.4731	0.56252	0.92815
H117	0.72544	0.36515	0.24416
H118	0.75053	0.32069	0.28067
H119	0.6759	0.26452	0.20183
H120	0.65125	0.30872	0.16466
H121	0.78131	0.19978	0.38836
H122	0.75879	0.244	0.34958
H123	0.82184	0.21078	0.24153
H124	0.84444	0.16657	0.28004
H125	0.67013	0.16847	0.27931
H126	0.71854	0.20334	0.24628
H127	0.67249	0.275	0.32265
H128	0.62445	0.24018	0.35649
H129	0.82883	0.29669	0.14854
H130	0.77799	0.26586	0.18524
H131	0.83828	0.28636	0.30048
H132	0.88872	0.31799	0.26421
Ru133	0	0	0.48125
Ru134	0.5	0.5	0.96784

Section 7. References

- [1] J. Jiao, Z. Li, Z. Qiao, X. Li, Y. Liu, J. Dong, J. Jiang, Y. Cui, *Nat. Commun.* 2018, **9**, 4423.
- [2] Y. Liu, C. S. Diercks, Y. Ma, H. Lyu, C. Zhu, *J. Am. Chem. Soc.* 2019, **141**, 677-683.
- [3] O. V. Dolomanov, L. J. Bourhis, R. J. Gildea, J. A. K. Howard, H. Puschmann, *J. Appl. Cryst.* 2009, **42**, 339-341.
- [4] G. M. Sheldrick, *Acta Cryst. A.* 2014, **70**, C1437.
- [5] G. M. Sheldrick, *Acta Cryst. C.* 2015, **71**, 3-8.
- [6] K. Nagoshi, S. Yamashita, M. Yagi, M. Kaneko, *J. Mol. Catal. A: Chem.* 1999, **144**, 71-76.
- [7] D. J. Wasylenko, C. Ganesamoorthy, B. D. Koivisto, M. A. Henderson, C. P. Berlinguette, *Inorg. Chem.* 2010, **49**, 2202-2209.
- [8] S. Maji, L. Vigara, F. Cottone, F. Bozoglian, J. Benet-Buchholz, A. Llobet, *Angew. Chem. Int. Ed.* 2012, **51**, 5967-5970.
- [9] C. Sens, I. Romero, M. Rodríguez, A. Llobet, T. Parella, J. Benet-Buchholz, *J. Am. Chem. Soc.* 2004, **126**, 7798-7799
- [10] L. Tong, A. K. Inge, L. Duan, L. Wang, X. Zou, L. Sun, *Inorg. Chem.* 2013, **52**, 2505-2518.
- [11] L. Tong, L. Duan, Y. Xu, T. Privalov, L. Sun, *Angew. Chem. Int. Ed.* 2011, **50**, 445-449.
- [12] M. Schulze, V. Kunz, P. D. Frischmann, F. Wurthner, *Nat. Chem.* 2016, **8**, 576-583.
- [13] L. Duan, F. Bozoglian, S. Mandal, B. Stewart, T. Privalov, A. Llobet, L. Sun, *Nat. Chem.* 2012, **4**, 418-423.
- [14] D. Schindler, M. Gil-Sepulcre, J. O. Lindner, V. Stepanenko, D. Moonshiram, A. Llobet, F. Wurthner, *Adv. Energy Mater.* 2020, **10**, 2002329.
- [15] N. Vereshchuk, M. Gil-Sepulcre, A. Ghaderian, J. Holub, C. Gimbert-Surinach, A. Llobet, *Chem. Soc. Rev.* 2023, **52**, 196-211.
- [16] B. Zhang, L. Sun, *J. Am. Chem. Soc.* 2019, **141**, 5565-5580.
- [17] M. J. Frisch, G. W. Trucks, H. B. Schlegel, G. E. Scuseria, M. A. Robb, J. R. Cheeseman, G. Scalmani, V. Barone, B. Mennucci, G. A. Petersson, H. Nakatsuji, M. Caricato, X. Li, H. P. Hratchian, A. F. Izmaylov, J. Bloino, G. Zheng, J. L. Sonnenberg, M. Hada, M. Ehara, K. Toyota, R. Fukuda, J. Hasegawa, M. Ishida, T. Nakajima, Y. Honda, O. Kitao, H. Nakai, T. Vreven, Jr. J. A. Montgomery, J. E. Peralta, F. Ogliaro, M. Bearpark, J. J. Heyd, E. Brothers, K. N. Kudin, V. N. Staroverov, R. Kobayashi, J. Normand, K. Raghavachari, A. Rendell, J. C. Burant, S. S. Iyengar, J. Tomasi, M. Cossi, N. Rega, J. M. Millam, M. Klene, J. E. Knox, J.B. Cross, V. Bakken, C. Adamo, J. Jaramillo, R. Gomperts, R. E. Stratmann, O. Yazyev, A. J. Austin, R. Cammi, C. Pomelli, J. Ochterski, R. L. Martin, K. Morokuma, V. G. Zakrzewski, G. A. Voth, P. Salvador, J. J. Dannenberg, S. Dapprich, A. D. Daniels, O. Farkas, J. B. Foresman, J. V. Ortiz, J. Cioslowski and D. J. Fox, Gaussian 09 (Revision E.01), Gaussian,

Inc., Wallingford, CT, 2013.

- [18] D. Moonshiram, J. W. Jurss, J. J. Concepcion, T. Zakharova, I. Alperovich, T. J. Meyer and Y. Pushkar, *J. Am. Chem. Soc.*, 2012, **134**, 4625-4636.
- [19] Y. He, G. Liu, Z. Liu, J. Bi, Y. Yu, L. Li, *ACS Energy Lett.* 2023, **8**, 1857-1863.
- [20] H. Chen, A. M. Gardner, G. Lin, W. Zhao, M. Bahri, N. D. Browning, R. S. Sprick, X. Li, X. Xu, A. I. Cooper, *Catal. Sci. Technol.* 2022, **12**, 5442-5452.
- [21] J. Xie, S. A. Shevlin, Q. Ruan, S. J. A. Moniz, Y. Liu, X. Liu, Y. Li, C. C. Lau, Z. X. Guo, J. Tang, *Energy Environ. Sci.* 2018, **11**, 1617-1624.
- [22] J. Bi, W. Fang, L. Li, J. Wang, S. Liang, Y. He, M. Liu, L. Wu, *Macromol. Rapid Commun.* 2015, **36**, 1799-1805.
- [23] S. Bi, C. Yang, W. Zhang, J. Xu, L. Liu, D. Wu, X. Wang, Y. Han, Q. Liang, F. Zhang, *Nat. Commun.* 2019, **10**, 2467.
- [24] J. Xu, C. Yang, S. Bi, W. Wang, Y. He, D. Wu, Q. Liang, X. Wang, F. Zhang, *Angew. Chem. Int. Ed.* 2020, **59**, 23845-23853.
- [25] D. Kong, X. Han, J. Xie, Q. Ruan, C. D. Windle, S. Gadipelli, K. Shen, Z. Bai, Z. Guo, J. Tang, *ACS Catal.* 2019, **9**, 7697-7707.
- [26] E. Jin, Z. Lan, Q. Jiang, K. Geng, G. Li, X. Wang, D. Jiang, *Chem.* 2019, **5**, 1632-1647.
- [27] C. Wang, H. Zhang, W. Luo, T. Sun, Y. Xu, *Angew. Chem. Int. Ed.* 2021, **60**, 25381-25390
- [28] Y. Wan, L. Wang, H. Xu, X. Wu, J. Yang, *J. Am. Chem. Soc.* 2020, **142**, 4508-4516.
- [29] R. S. Sprick, Z. Chen, A. J. Cowan, Y. Bai, C. M. Aitchison, Y. Fang, M. A. Zwijnenburg, A. I. Cooper, X. Wang, *Angew. Chem. Int. Ed.* 2020, **59**, 18695-18700.
- [30] Y. Yang, X. Chu, H. Y. Zhang, R. Zhang, Y. H. Liu, F. M. Zhang, M. Lu, Z. D. Yang, Y. Q. Lan, *Nat. Commun.* 2023, **14**, 593.
- [31] J. Qiao, Z. Song, C. Huang, R. Ci, Z. Liu, B. Chen, C. Tung, L. Wu, *Angew. Chem., Int. Ed.* 2021, **60**, 27201-27205.
- [32] X. Xiao, Z. Ruan, Q. Li, L. Zhang, H. Meng, Q. Zhang, H. Bao, B. Jiang, J. Zhou, C. Guo, X. Wang, H. Fu, *Adv. Mater.* 2022, **34**, e2200612.